Ore Geology Reviews 89 (2017) 421–440

Contents lists available at ScienceDirect

Ore Geology Reviews

journal homepage: www.elsevier.com/locate/oregeo

Geology, fluid inclusion and isotope constraints on ore genesis of the post-collisional Dabu porphyry Cu–Mo deposit, southern Tibet

Song Wu [a], Youye Zheng [a,b,*], Ruirui Geng [c], Liangxu Jin [e], Bo Bao [d], Meng Tan [a], Feng Guo [a]

[a] State Key Laboratory of Geological Processes and Mineral Resources, and School of Earth Science and Resources, China University of Geosciences, Beijing 100083, China
[b] State Key Laboratory of Geological Processes and Mineral Resources, and Faculty of Earth Resources, China University of Geosciences, Wuhan 430074, China
[c] Beijing Research Institute of Uranium Geology, Beijing 100029, China
[d] Wuhan Center, China Geological Survey, Wuhan 430205, China
[e] No. 2 Geological Party, Bureau of Geology and Mineral Exploration and Development, Lhasa 850007, Tibet, China

ARTICLE INFO

Article history:
Received 16 January 2017
Received in revised form 26 June 2017
Accepted 30 June 2017
Available online 3 July 2017

Keywords:
Fluid inclusion
Ore-forming conditions
Post-collisional porphyry deposit
Dabu
Tibet

ABSTRACT

The Dabu Cu-Mo porphyry deposit is situated in the southern part of the Lhasa terrane within the post-collisional Gangdese porphyry copper belt (GPCB). It is one of several deposits that include the Qulong and Zhunuo porphyry deposits. The processes responsible for ore formation in the Dabu deposit can be divided into three stages of veining: stage I, quartz–K-feldspar (biotite) ± chalcopyrite ± pyrite, stage II, quartz–molybdenite ± pyrite ± chalcopyrite, and stage III, quartz–pyrite ± molybdenite. Three types of fluid inclusions (FIs) are present: liquid-rich two-phase (L-type), vapor-rich two-phase (V-type), and solid bearing multi-phase (S-type) inclusions. The homogenization temperatures for the FIs from stages I to III are in the ranges of 272–475 °C, 244–486 °C, and 299–399 °C, and their salinities vary from 2.1 to 49.1, 1.1 to 55.8, and 2.9 to 18.0 wt% NaCl equiv., respectively. The coexistence of S-type, V-type and L-type FIs in quartz of stage I and II with similar homogenization temperatures but contrasting salinities, indicate that fluid boiling is the major factor controlling metal precipitation in the Dabu deposit. The ore-forming fluids of this deposit are characterized by high temperature and high salinity, and they belong to a H_2O–NaCl magmatic–hydrothermal system. The H–O–S–Pb isotopic compositions indicate that the ore metals and fluids came primarily from a magmatic source linked to Miocene intrusions characterized by high Sr/Y ratios, similar to other porphyry deposits in the GPCB. The fluids forming the Dabu deposit were rich in Na and Cl, derived from metamorphic dehydration of subducted oceanic slab through which NaCl-brine or seawater had percolated. The inheritance of ancient subduction-associated arc chemistry, without shallow level crustal assimilation and/or input of the meteoric water, was responsible for the generation of fertile magma, as well as CO_2-poor and halite-bearing FIs associated with post-collisional porphyry deposits. The estimated mineralization depths of Qulong, Dabu and Zhunuo deposits are 1.6–4.3 km, 0.5–3.4 km and 0.2–3.0 km, respectively, displaying a gradual decrease from eastern to western Gangdese. Deep ore-forming processes accounted for the generation of giant-sized Qulong deposit, because the exsolution of aqueous fluids with large fraction of water and chlorine in deep or high pressure systems can extract more copper from melts than those formed in shallow systems. However, the formation of small-sized Dabu deposit can be explained by a single magmatic event without additional replenishment of S, metal, or thermal energy. In addition, the ore-forming conditions of porphyry Cu–Mo deposits in GPCB are comparable to those of porphyry Cu ± Au ± Mo deposits formed in oceanic subduction-related continental or island arcs, but differ from those of porphyry Mo deposit formed in the Dabie-Qinling collisional orogens. The depth of formation of the mineralization and features of primary magma source are two major controls on the metal types and ore-fluid compositions of these porphyry deposits.

1. Introduction

The porphyry deposits, particularly giant ones, are the results of an optimal alignment and combinations of tectonic controls, host rock types, and focused flow of fluids (Richards, 2013). Their

* Corresponding author at: State Key Laboratory of Geological Processes and Mineral Resources, and School of Earth Science and Resources, China University of Geosciences, Beijing 100083, China.
E-mail address: zhyouye@163.com (Y. Zheng).

http://dx.doi.org/10.1016/j.oregeorev.2017.06.030
0169-1368/

formation is generally associated with Cu-rich and/or anomalously S-rich parental melts with high oxygen fugacity and water content formed under magmatic conditions (Halter et al., 2005; Core et al., 2006; Sillitoe, 2010; Richards, 2011a, 2011b; Sun et al., 2013a; Loucks, 2014; Lu et al., 2015). Recently, many porphyry copper deposits have been discovered along the non-arc or post-collisional setting of the eastern Tethys; examples include the deposits in the Kerman porphyry Cu belt in Iran (Fig. 1a; Shafiei et al., 2009; Richards et al., 2012) and the Gangdese porphyry Cu–Mo belt (GPCB) in Tibet, China (Fig. 1a; Zheng et al., 2004; Hou et al., 2009). These deposits are geochemically associated with rocks formed from adakite-like calc-alkaline (Jahangiri, 2007; Shafiei et al., 2009; Asadi et al., 2014) or high-K calc-alkaline and shoshonitic magmas (Chung et al., 2005; Qu et al., 2007; Hou et al., 2011).

The GPCB, located on the northern margin of the Indus–Yarlung Zangbo suture zone, is regarded as one of the most richly endowed copper provinces in the Alpine–Himalayan orogenic belt (Fig. 1b; Mao et al., 2014; Hou and Zhang, 2015; Zheng et al., 2015a). In GPCB, there are numerous porphyry Cu–Mo deposits that formed in a post-collisional setting, such as Qulong, Zhunuo, and Dabu (Fig. 1b; Zheng et al., 2004, 2007, 2014; Yang, 2008; Yang et al., 2009; Wu et al., 2014, 2016).

The world-class giant Qulong porphyry Cu-Mo deposit, firstly described by Zheng et al. (2004), Gao and Zheng (2006) and Zheng et al. (2006), is situated in the central segment of south Lhasa terrane about 50 km eastern of Lhasa (Fig. 1b). This deposit contains >10 Mt Cu and 0.44 Mt Mo at an average grade of 0.44% and 0.02%, respectively (Zheng et al., 2015a). Metal reserves are expected to increase as a result of exploration in the periphery and at depth. The Qulong Cu–Mo deposit is associated with the stock-shaped Miocene intrusive complex, with an outcrop area of 8 km^2 and ages ranging from 19.6 Ma to 15.7 Ma. Mafic enclaves and magmatic anhydrite are commonly present (Yang, 2008; Xiao et al., 2012; Zheng et al., 2013). The Zhunuo deposit is a large-sized porphyry Cu-Mo deposit in the western segment of south Lhasa terrane which is located about approximately 165 km western of Xigaze (Fig. 1b). This deposit contains reserves of 2.3 Mt Cu at an average grade of 0.57% (Zheng et al., 2015a). The mineralization-associated monzogranite porphyry at the Zhunuo deposit has a zircon U–Pb age of 14.4 ± 0.2 Ma (Zheng et al., 2014), similar to molybdenite Re–Os age of 13.7 ± 0.6 Ma (Zheng et al., 2007). The Dabu deposit in the southern part of the Lhasa terrane is a porphyry Cu-Mo deposit formed in a post-collisional setting in the GPCB, which is classified as small-sized porphyry-type deposit with a reserve of approximately 0.5 Mt Cu at an average grade of ~0.31 wt% (Zheng et al., 2015a). The geology, geochemistry, and geochronology of post-subduction porphyry deposits in the GPCB have been extensively studied (Zheng et al., 2002, 2015a; Qu et al., 2004, 2007; Yang et al., 2009, 2015a; Qin, 2012; Wang et al., 2014a, 2014b, 2014c, 2015a; Hou et al., 2015b; Lu et al., 2015; Wu et al., 2016). However, little is actually known regarding the key controls on the diversity in scale of deposits in the GPCB (e.g., giant, large, small; Fig. 1b). Due to a lack of systematic fluid inclusion studies, the ore-forming process, as well as the characteristics and source of ore metals and fluids, compared to porphyry deposits formed in magmatic arc settings (Bodnar et al., 2014), are still poorly understood (Hou et al., 2009; Landtwing et al., 2010), which undermines efforts to model the porphyry-style ore deposits in the GPCB.

The Dabu deposit is a small-sized porphyry Cu-Mo deposit in GPCB. Previous studies were mainly focused on geochronology and geochemistry (Wu et al., 2014, 2016). However, an integrated study of the fluid evolution and source of the Dabu deposit have so far not been reported. Fluid inclusions (FIs), as the record of ore-forming fluids, are critical for understanding the physical and

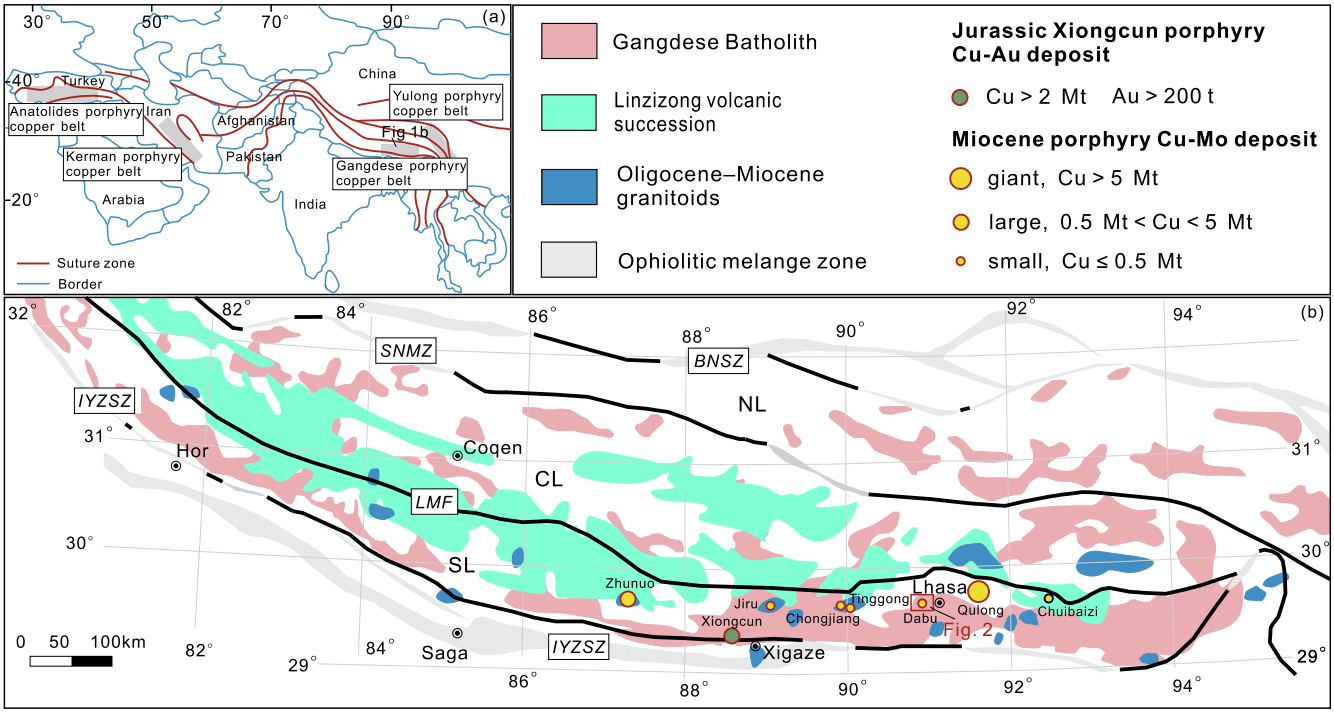

Fig. 1. (a) Distribution of some collision-related porphyry copper belts in the Alpine–Himalayan orogenic belt (modified after Singer et al., 2005 and Hou et al., 2011); (b) simplified geologic map of the Lhasa terrane showing the distribution of major porphyry deposits and the location of the study area (modified after Mo et al., 2008; Zhu et al., 2011a and Wu et al., 2014). The three kinds of yellow circles denote different size of porphyry deposits. Abbreviations: BNSZ–Bangong-Nujiang suture zone, SNMZ–Shiquan River-Nam Tso Mélange Zone, LMF–Luobadui-Milashan Fault, IYZSZ–Indus-Yarlung Zangbo Suture Zone, SL–southern Lhasa subterrane, CL–central Lhasa subterrane, NL–northern Lhasa subterrane. (For interpretation of the references to colour in this figure legend, the reader is referred to the web version of this article.)

chemical nature and transportation–deposition mechanisms of fluids in porphyry deposits (Wilkinson, 2001). In this contribution, we have carried out geologic, fluid inclusion, and systematic H–O–S–Pb isotope studies of the Dabu deposit. Petrography coupled with microthermometry and Laser Raman microspectroscopy analyses of FIs in quartz were used to determine volatile components and trapping temperatures of the ore-forming fluid. The trapping pressure of fluid and mineralization depths were also estimated, and compared with Qulong and Zhunuo porphyry deposits in GPCB, as well as other typical porphyry deposits formed in subduction and intracontinental collision zones. We present a model for the genesis of post-collisional porphyry Cu-Mo deposits in Tibet.

2. Geological setting and regional geology

The Tibetan Plateau formed as a result of the Indian–Asian continental collision in Early Tertiary, is a complex tectonic collage of several accreted terranes, which include the Songpan–Ganzi, Qiangtang, Lhasa, and Himalaya terranes from north to south (Yin and Harrison, 2000). The Lhasa terrane, bounded by the Bangong–Nujiang and Indus–Yarlung Zangbo sutures, is a ~2500-km-long tectono–magmatic belt with a width of ~150–300 km (Fig. 1b; Pan et al., 2006). It is composed of Precambrian crystalline basement unconformably overlain by Paleozoic to Mesozoic marine strata and arc-type volcanic rocks, abundant Mesozoic and Cenozoic intrusions, and three medium- to high-grade metamorphic belts (Yin and Harrison, 2000; Pan et al., 2006; Dong et al., 2010; Zhu et al., 2013; Zhang et al., 2014). Accordingly, the Lhasa terrane can be further subdivided into the northern, central, and southern subterranes that are separated by the Shiquanhe–Nam Tso Mélange Zone and the Luobadui–Milashan Fault (Fig. 1b; Pan et al., 2004, 2006; Zhu et al., 2011a).

The central Lhasa subterrane represents a microcontinent derived from either the Australian or Indian parts of Gondwana with Precambrian basement rocks (Yin and Harrison, 2000; Zhu et al., 2011b), part of which have undergone multiple episodes of metamorphism (Zhang et al., 2014). This reworked crystalline basement is covered by a discontinuous widespread blanket of Carboniferous–Permian metasedimentary rocks and Upper Jurassic–Lower Cretaceous sedimentary rocks with abundant volcanic rocks (Pan et al., 2004; Zhu et al., 2009, 2011a, 2013), and minor small-volume Tertiary granitoids (Zheng et al., 2015b). The ore deposits that occur within the central Lhasa subterrane are mainly porphyry or skarn Mo(–W–Cu), skarn Pb–Zn(–Ag), and skarn Fe(–Cu) deposits such as Yaguila, Mengya'a, Narusongduo, Qiagong, Hahaigang and Sharang. These deposits form the northeastern Gangdese Pb–Zn–Ag–Fe–Mo–W polymetallic belt (Li et al., 2011a, 2014a; Zhao et al., 2014; Hou et al., 2015a; Zheng et al., 2015a).

In contrast, the southern and northern Lhasa subterranes are characterized by juvenile crust resulted from the under-plating of mantle-derived magmas during the Mesozoic and Cenozoic periods with a locally preserved Precambrian crystalline basement (Ji et al., 2009; Zhu et al., 2011a; Hou et al., 2015a). The northern Lhasa subterrane is underlain by Neoproterozoic or Cambrian crystalline basement which is exposed in the Amdo region (Xu et al., 1985; Dewey et al., 1988; Guynn et al., 2012). This subterrane is covered by Middle Triassic–Cretaceous sedimentary rocks with abundant Early Cretaceous volcanic rocks and associated granitoids (cf. Pan et al., 2004; Zhu et al., 2013). In the southern Lhasa subterrane, magmatic activities are represented by the widespread Gangdese batholith (205~41 Ma) and Linzizong volcanic successions (65–43 Ma). These igneous rocks make up an Andean-style magmatic arc (Fig. 1b), that formed in response to the northward subduction of Tethyan oceanic lithosphere, slab rollback and subsequent break–off (Mo et al., 2008; Wen et al., 2008; Ji et al., 2009; Lee et al., 2012a).

With the continuous convergence of India with Asia, the post-collisional magmatism developed in the central and southern Lhasa subterranes consists of mantle-derived ultra-potassic and potassic volcanic rocks, along with high Sr/Y granitoid rocks (cf. Chung et al., 2005; Liu et al., 2017). Ultra-potassic rocks have ages ranging from 24 to 10 Ma and usually occur as lava flows cropping out throughout the central Lhasa subterrane (Turner et al., 1996; Miller et al., 1999; Williams et al., 2004; Zhao et al., 2009; Liu et al., 2014a; Guo et al., 2015). Miocene potassic volcanic rocks are mainly distributed in the central and southern Lhasa subterranes, with eruptive ages coeval with the Tibetan ultra-potassic rocks (Miller et al., 1999; Nomade et al., 2004; Chung et al., 2005). High Sr/Y Oligocene–Miocene granitic rocks are commonly present as small-volume intrusions or dykes, cutting the Gangdese batholith and associated syn-collisional volcanic rocks (Fig. 1b; Chung et al., 2009; Gao et al., 2010; Zheng et al., 2012a). The post-collisional porphyry Cu-Mo deposits concentrated in the southern Lhasa subterrane are generally associated with high Sr/Y Miocene intrusions, and they define the giant Gangdese porphyry Cu belt that includes the Zhunuo, Jiru, Chongjiang, Tinggong, Dabu, Lakang'e, Qulong, Demingding, Chuibaizi, and Tangbula deposits (Fig. 1b). All of these deposits have molybdenite Re–Os ages between ca. 21 and 13 Ma and are associated with ca. 20 and 13 Ma intrusions (Zheng et al., 2015a). Several porphyry–skarn Cu–W–Mo deposits (e.g., Mingze–Chengba and Nuri), located within the SE margin of the Gangdese belt, are related to Oligocene granodiorite or monzonite intrusions (Sun et al., 2013b; Chen et al., 2015).

3. Deposit geology

The Dabu porphyry Cu–Mo deposit is located ~40 km west of Lhasa in southern Tibet at geographic coordinates 90°48′E and 29°31′N (Fig. 2). The mineralization age of the deposit is ca. 14.8 ± 0.2 Ma, as constrained from Re–Os isotopic dating of molybdenite (Qu et al., 2007), and is coeval with the monzogranite porphyry based on SHRIMP U–Pb isochron dating of zircon (14.6 ± 0.4 Ma) (Wu et al., 2014). These ages indicate that the Dabu porphyry deposit was formed in a post-collisional setting. There are two orebodies in the deposit with a surface outcrop area of ca. 1.5 km^2, where the mineralization is genetically associated with the Miocene monzogranite porphyry (Fig. 2). The main geologic units in the Dabu district include Eocene monzogranite, porphyritic monzogranite, granodiorite and Miocene monzogranite porphyry (Fig. 2). The Eocene medium- to coarse-grained biotite monzogranite, porphyritic monzogranite and gray–white granodiorite are widespread throughout the area, and are intruded by smaller stocks or dykes of the Miocene monzogranite porphyry (Fig. 2). Ovoidal and ellipsoidal mafic microgranular enclaves are present in the Miocene monzogranite (Wu et al., 2014). The unaltered Eocene rocks are light red in colour, and contain K-feldspar, plagioclase, quartz, as well as minor hornblende and biotite. The K-feldspar crystals range from 10 to 30 mm in size, forming euhedral megacrysts, whereas the plagioclase, quartz, hornblende, and biotite forming the crystalline groundmass of the rock are subhedral to anhedral. Hornblende is usually present as small crystals within K-feldspar phenocrysts, indicating that it crystallized after the feldspars in more evolved melts (Wu et al., 2016). The Miocene monzogranite porphyry contains quartz, plagioclase, K-feldspar, and biotite phenocrysts that range in size from 1 to 4 mm, as well as minor amounts of magnetite, ilmenite, apatite, rutile, and sphene phenocrysts. The groundmass is microcrystalline or consists of aphanitic felsic minerals (Wu et al., 2016). Alteration assemblages in the Dabu deposit are similar to those observed in other porphyry Cu deposits worldwide, including potassium

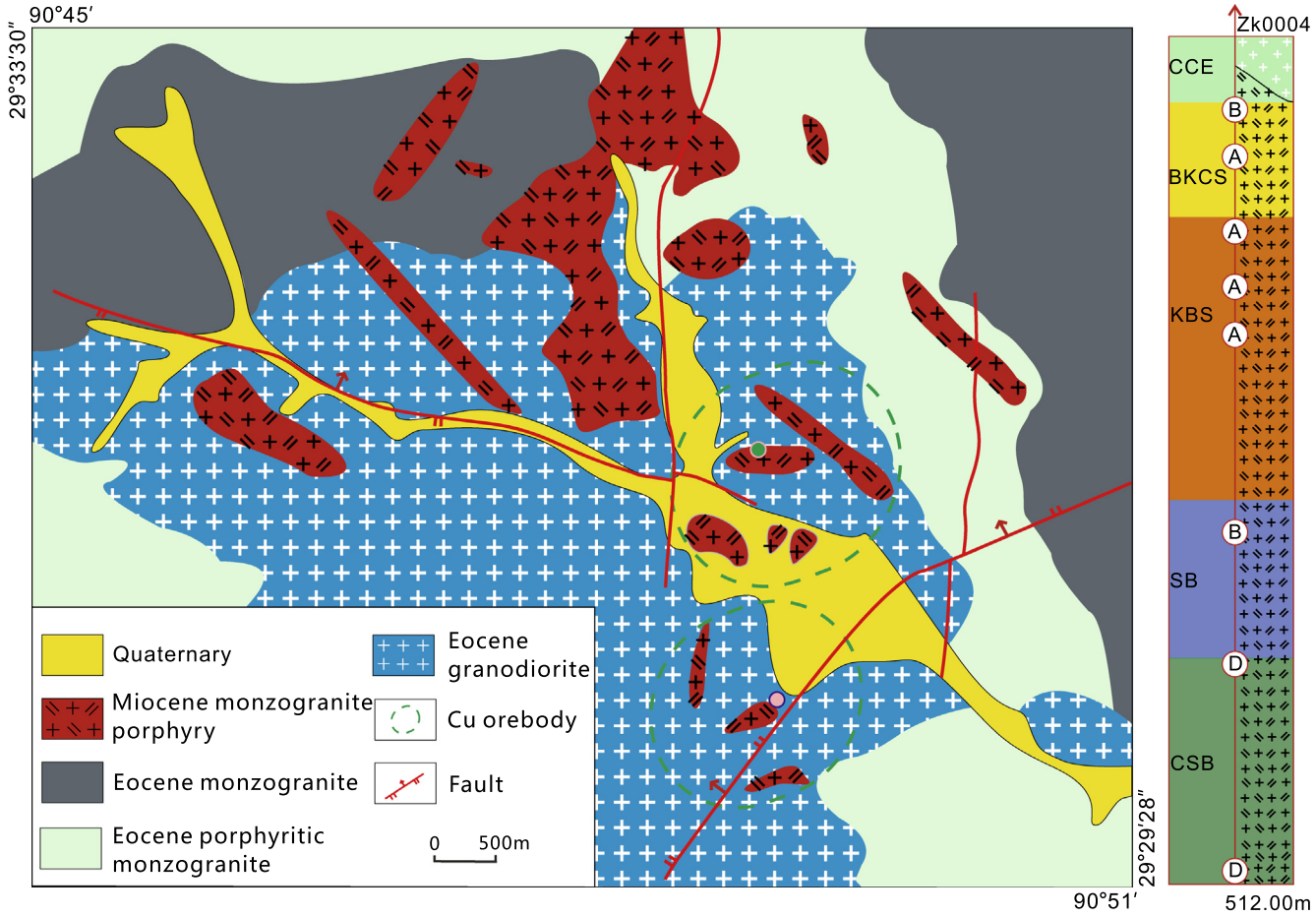

Fig. 2. Geological map of the Dabu porphyry Cu–Mo deposit, lithologic column and alteration assemblages of drill hole Zk0004 (modified after Geologic Exploration Team of Geological Survey Institute of Tibet, 2011). The pink circle in the map denotes the location of drill hole Zk0004. The locations of samples chosen for fluid inclusions study are labelled by circle in the column and others sampled from surface are marked by green circle on the map. The text in the circles denotes the vein types. Abbreviations: CCE–clay-chlorite-epidote alteration, BKCS–biotite-k-feldspar-chlorite-sericite alteration, KBS–k-feldspar-biotite-sericite alteration, SB–sericite-biotite alteration, CSB–chlorite-sericite-biotite alteration, anh–anhydrite. (For interpretation of the references to colour in this figure legend, the reader is referred to the web version of this article.)

silicate (potassic), phyllic (sericitic), propylitic and intermediate argillic (Meyer et al., 1967). The ore minerals associated with both phyllic and potassic alterations at the Dabu deposit are hosted in the monzogranite porphyry.

Based on field observation, cross-cutting relationships and petrography, a three-stage paragenetic sequence has been proposed that consists of A, B, and D type veins from early to late (Gustafson and Quiroga, 1995; Sillitoe, 2010). Alteration and mineralization paragenesis is documented in Fig. 3.

Stage I (also called A vein) is represented by quartz–K-feldspar ± chalcopyrite ± pyrite and quartz–biotite ± chalcopyrite ± pyrite veinlets or veins. These veins are asymmetric in form, accompanied by alteration halos of K-feldspar and biotite that are usually inconspicuous and discontinuous (Fig. 4). The quartz–K-feldspar veins commonly lack of sulfides and cut by stage II quartz veinlet, but disseminated chalcopyrite occurs in clusters of secondary biotite around the quartz–K-feldspar veinlets (Fig. 4a, b, c). The quartz–K-feldspar–pyrite–chalcopyrite veins are cut by stage II quartz veinlets that are associated with sericitic alteration assemblage (Fig. 4d). The quartz–biotite–chalcopyrite–pyrite veinlet is cut by stage III quartz–pyrite veinlet that is associated with propylitic alteration assemblage (Fig. 4f). The chalcopyrite in the biotite-bearing veinlets is generally anhedral with diameter <100μm (Fig. 4g). Despite sulfides in vein or veinlet, disseminated chalcopyrite on fracture and star-like distributed chalcopyrite in rocks can also be observed, along with minor amounts of pyrite, bornite and molybdenite (Fig. 4h, i). The alteration type in stage I is dominated by potassium-silicate, which is represented by the formation of K-feldspar, biotite, and quartz. The K-feldspar alteration is characterized by the presence of disseminated secondary fine-grained K-feldspar crystals, quartz-K-feldspar veinlets (Fig. 4a, b), fine-grained K-feldspar crystals that occur discontinuously at the vein or veinlet margins (Fig. 4c) or micro-grains of K-feldspar in alteration halos around K-feldspar phenocryst (Fig. 4j). The clusters of anhedral biotite together with fine-grained quartz along the veinlet form a glomeroporphyritic texture (Fig. 4b, c), replacement of primary biotite or amphibole by thin flakes of secondary biotite is observed in the rock matrix (Fig. 4k), and irregular biotite veinlets(Fig. 4l) are the main styles of biotite alteration.

Stage II (also called B vein) can be represented by quartz ± pyrite ± chalcopyrite (Fig. 5a, b, c) and quartz–molybdenite ± pyrite ± chalcopyrite (Fig. 5d, e) veins. This stage is characterized by the formation of relatively coarse-grained quartz and symmetrical veins, along which the alteration halos are absent or occur as occasionally faint and irregular bleached halos (Fig. 5). Sulfides in this stage are mainly associated with phyllic alteration and are dominated by molybdenite and pyrite with minor chalcopyrite and magnetite. The dominant molybdenite is either concentrated in bands parallel to vein walls and mostly occur at the centerlines and margins of such veins (Fig. 5d, e), or disseminated in cracks (Fig. 5f). Minor amounts of chalcopyrite have a subhedral

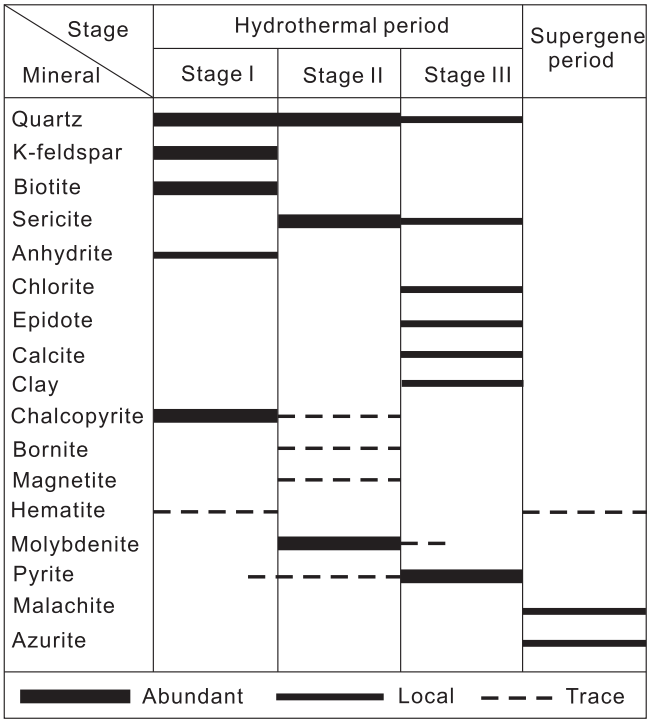

Fig. 3. Mineral paragenesis for the Dabu porphyry Cu–Mo deposit.

shape intergrowth with lamellar molybdenite, pyrite and ragged magnetite (Fig. 5g, h). Phyllic alteration is characterized by the development of sericitic alteration selvages along the margins of ore-bearing vein or veinlets (Fig. 5b) and selective replacement of feldspar phenocryst by fine-grained, scaly–acicular to anhedral sericite (Fig. 5i).

Stage III (also called D vein) is represented by quartz–pyrite ± molybdenite veins associated with propylitic alteration (Fig. 6). These veins are commonly irregular in shape with a width ranging from 2 to 20 mm (Fig. 6a, b, c). In this stage, pyrite is usually the predominant sulfide and molybdenite occurs locally. Pyrite occurs in two main modes: subhedral to euhedral pyrite (Fig. 6e) in quartz–pyrite veins (Fig. 6a, b, c) and disseminated pyrite along cracks (Fig. 6d). Propylitic alteration is characterized by chlorite and sericitic halos along the pyrite-bearing vein or veinlet (Fig. 6c, f), epidote veinlet (Fig. 6g), local replacement of feldspar or biotite phenocryst by fine- to medium-grained epidote and chlorite (Fig. 6h), and lesser amounts of calcite. Intermediate argillic alteration only occurs in shallow surface and is dominated by selective pervasive replacement of feldspar by clay minerals (Fig. 6i).

4. Sampling and analytical methods

4.1. Fluid inclusion analytical methods

Samples for the fluid inclusion study include ore-bearing or barren A, B, D type veins from stage I, II, III, respectively, and detailed sampling locations as well as their alteration assemblages are shown in Fig. 2. Microthermometry was performed at the Resources Exploration Laboratory, China University of Geosciences, Beijing. Microthermometric measurement was carried out on a Linkam THMS 600 heating–freezing stage attached to a Zeiss microscope, which has a measured temperature range of −196 °C to +600 °C. Freezing and heating runs were undertaken using liquid nitrogen and a thermal resistor, respectively. The ice-melting temperature ($T_{m,\ ice}$) and total homogenization temperatures of fluid phases ($T_{h,\ total}$) in FIs were recorded. The heating rate was maintained at about 5 °C per minute during the initial stages of each heating run and reduced to 0.1 °C per minute when the phase transitions were approached. The sample preparation and microthermometric analysis of FIs followed procedures described in Shepherd et al. (1985).

Compositions of individual FIs in quartz, including gas, liquid, and daughter mineral phases, were analyzed using the Renishaw MK1-1000 Laser Raman microspectrometer at the State Key Laboratory of Geological Process and Mineral Resources, China University of Geosciences, Wuhan. An Ar^+ laser with a wave length of 532 nm was used as the laser source with a power of 22 mW. The spectrum diagram was taken from the wave band of 100–4000 cm^{-1}. The spectral resolution was ±2 cm^{-1} with a beam size of 1 μm. The instrumental settings were kept constant during the analysis.

4.2. H-O isotope analytical methods

Ten quartz samples from A, B, D types of quartz–sulfide veins in stage I, II, III were collected for hydrogen and oxygen isotope analyses. Hydrogen and oxygen isotopic compositions of the quartz were measured using a MAT 253EM mass spectrometer at the Institute of Mineral Resources, Chinese Academy of Geological Sciences, Beijing. The BrF_5 method of Clayton and Mayeda (1963) was used to generate oxygen that was converted to CO_2 by reaction with a carbon rod. Water from fluid inclusion samples was collected by thermal decrepitation of quartz under vacuum at 500 °C and then reduced over Zn at 400 °C to generate H_2 (Coleman et al., 1982). The stable isotope results are reported relative to the V-SMOW standard, with an analytical errors of ±0.2‰ for $\delta^{18}O$ and ±2‰ for δD, respectively.

4.3. S-Pb isotope analytical methods

Seventeen sulfide samples including pyrite, chalcopyrite and molybdenite from the Dabu porphyry Cu–Mo deposit were selected for sulfur isotope analyses. Separates of sulfide minerals from different stages were prepared with careful handpicking under a binocular microscope to achieve a purity of 98%. The sulfur isotopic compositions were determined at the Analytical Laboratory of Beijing Research Institute of Uranium Geology. The sulfide grains were mixed with cuprous oxide and crushed into 200 mesh powder. SO_2 was produced through the reaction of sulfide and cuprous oxide at 980 °C under a vacuum pressure of 2×10^{-2} Pa (Robinson and Kusakabe, 1975). The SO_2 was then measured by MAT-251 mass spectrometer for sulfur isotope. All of the analytical uncertainties were better than ±0.2‰.

The lead isotope analysis of seven mineral separates of molybdenite and pyrite were carried out using a GV Isoprobe-T thermal ionization mass spectrometer (TIMS) at the Analytical Laboratory of Beijing Research Institute of Uranium Geology. All Pb ratios were corrected according to the values of NBS SRM 981. The lead isotope analytic errors were reported as ±2σ, and the measurement accuracy was better than 0.005% for $^{208}Pb/^{206}Pb$ and $^{204}Pb/^{206}Pb$ values.

5. Fluid inclusion results

5.1. Petrography

Based on the compositions of FIs and phases (L–V–S) at room temperature (25 °C), phase transitions observed during heating and cooling, and Laser Raman spectroscopy, three types of FIs were recognized in the studied quartz samples from Dabu, which are shown in Fig. 7, and are described below.

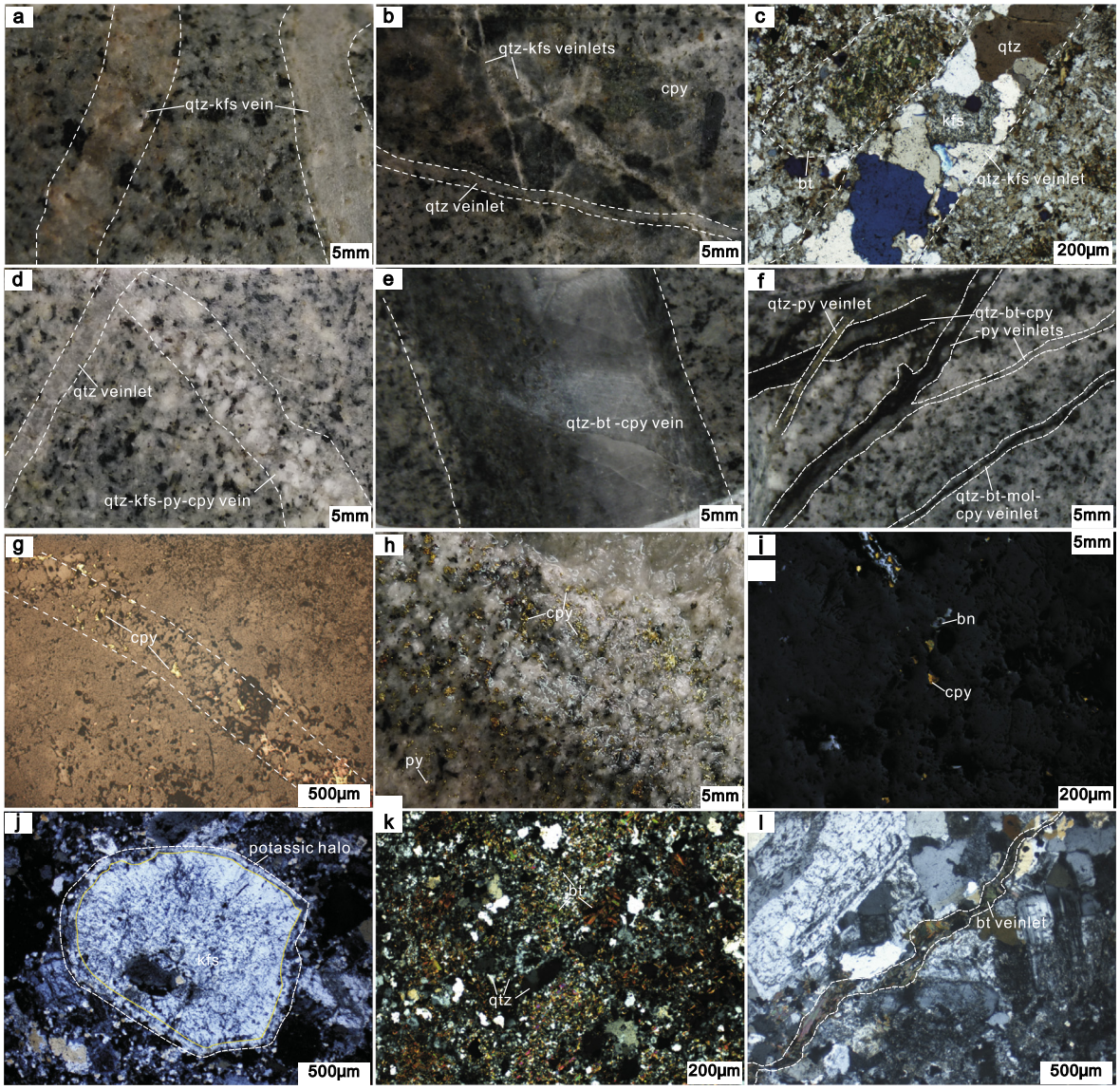

Fig. 4. Vein types, alteration and mineralization mineral assemblages of stage I at Dabu Cu-Mo deposit. (a) quartz–K-feldspar vein; (b) quartz–K-feldspar veinlets cut by stage II quartz veinlet, showing that fine-grained chalcopyrite occurs as clots within secondary quartz and biotite; (c) quartz–K-feldspar veinlet was locally surrounded by clusters of anhedral secondary biotite; (d) quartz–K-feldspar–pyrite–chalcopyrite vein cut by stage II quartz veinlet; (e) quartz–biotite–chalcopyrite vein displaying biotite and silicic halos banding parallel to the vein; (f) irregular quartz–biotite–molybdenite–chalcopyrite and quartz–biotite–chalcopyrite–pyrite veinlets cut by stage III quartz–pyrite veinlet; (g) anhedral chalcopyrite in the biotite-bearing veinlet; (h) sparsely disseminated chalcopyrite and pyrite; (i) star-like distributed bornite and chalcopyrite; (j) micro-grain potassic alteration halo growth around the K-feldspar phenocryst; (k) mineral assemblages of anhedral biotite and fine-grained quartz; (l) irregular biotite veinlet. Abbreviations: qtz–quartz, bt–biotite, kfs–K-feldspar, bn–bornite, py–pyrite, cpy–chalcopyrite, mol–molybdenite.

Vapor-rich two-phase FIs (V-type) are two-phase fluid system at room temperature, with >45 vol% of vapor bubbles and rarely present as monophase vapor inclusions (Fig. 7a, b, c). These inclusions typically have negative crystal or ellipse shape and are normally 5–25 μm in diameters. They generally occur in clusters or distribute randomly in the veins of stage I and II, which account for about 44% of the total FIs.

Liquid-rich two-phase FIs (L-type) contain a liquid phase and a vapor bubble without daughter crystals at room temperature. Liquid-rich L-type FIs occur commonly in all veins but are most abundant in stage II quartz, with <45 vol% of vapor bubbles and homogenization to a liquid phase. These inclusions are elongate or irregular in shape ranging from 4 to 25 μm in diameters (Fig. 7i), and account for approximately 45% of the total FIs.

Solid bearing multi-phase FIs (S-type) consist of one or more daughter minerals, aqueous solution, and a vapor bubble. These inclusions generally vary from 4 to 24 μm in size with negative crystal or polygonal shapes, and account for 11% of the observed FIs. The S-type inclusions are typically present in stages II quartz veins, as well as in stage I quartz associated with biotite alteration, coexisting with V-type and L-type FIs (Fig. 7b). The most common daughter minerals are transparent, including cubic halite (Fig. 7e, f, g), elongated apatite (Fig. 7h) and round sylvite crystals. Minor amounts of opaque chalcopyrite (Fig. 7d, e) and hematite (Fig. 7g) are also observed. Based on the homogenous nature of the daughter minerals, the S-type FIs can generally be divided into two types: the daughter mineral of type S1 dissolves before vapor disappearance and the dissolution of type S2 occurs later than vapor disappearance upon heating.

5.2. Laser Raman spectroscopy

The results of Laser Raman microspectroscopic analyses of individual FIs are shown in Fig. 8. It can be generally recognized that

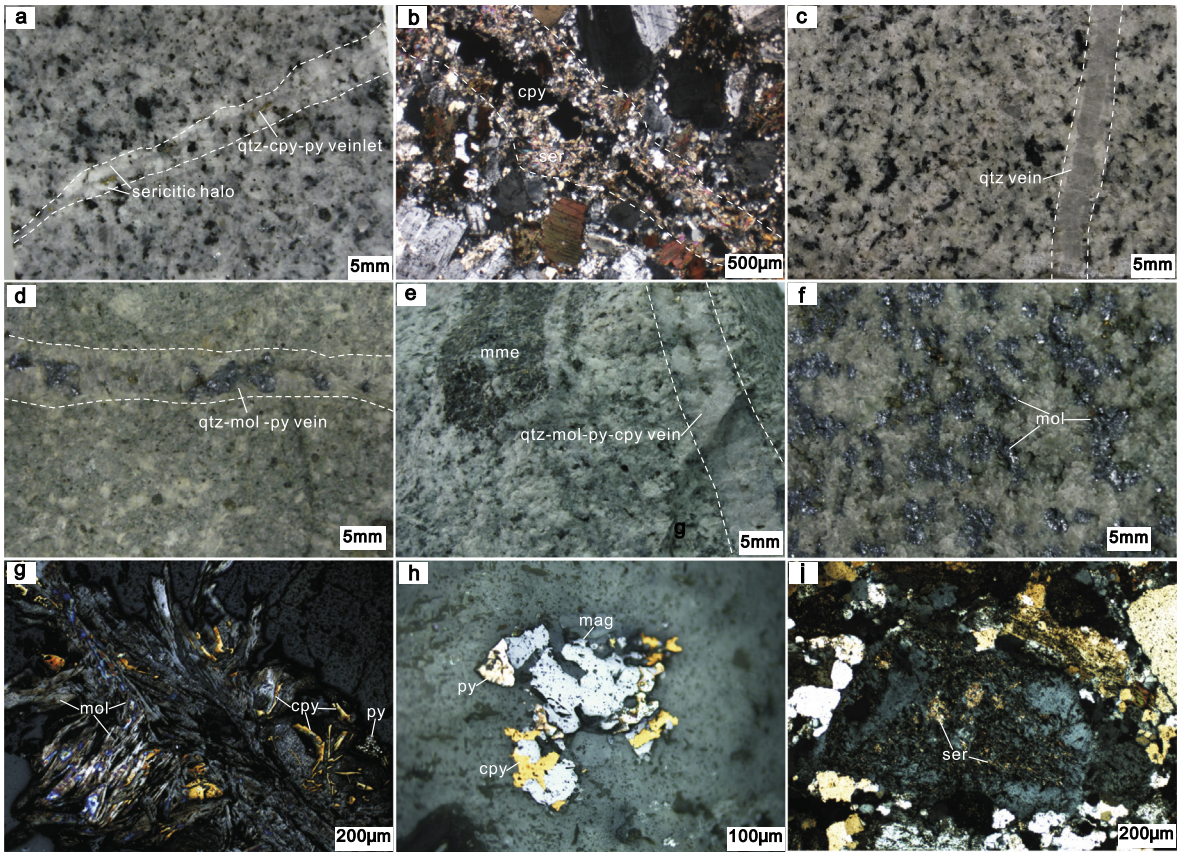

Fig. 5. Vein types, alteration and mineralization mineral assemblages of stage II at Dabu Cu-Mo deposit. (a) quartz–chalcopyrite–pyrite veinlet surrounded by sericitic halo; (b) quartz–chalcopyrite–pyrite veinlet showing sericitic alteration halo along its margins; (c) quartz vein showing typical vein symmetry; (d) quartz–molybdenite–pyrite vein; (e) quartz–molybdenite–pyrite–chalcopyrite vein characterized by the filling of sulfides along the centerlines and margins; (f) molybdenite occurs as disseminations in cracks; (g) clusters of anhedral chalcopyrite, pyrite and lamellar molybdenite; (h) anhedral-granular chalcopyrite intergrowth with magnetite and pyrite; (i) selective replacement of feldspar phenocryst by fine-grained sericite. Abbreviations: qtz–quartz, py–pyrite, cpy–chalcopyrite, mol–molybdenite, mag–magnetite, ser–sericite, mme–mafic microgranular enclaves.

H_2O dominates the liquid phase, while CO_2 can only be identified in vapor bubbles. Sometimes in the Raman spectra for the solid phase of S-type FIs in stage II, the peak of 288, 352 cm^{-1} and 291, 410, 1319 cm^{-1} were observed.

5.3. Microthermometry

As stated above, CO_2 is identified in vapor bubbles of two phases FIs by laser Raman, but CO_2-bearing three phases FIs were not observed at room temperature and during freezing in this study, thus CO_2 only occurs as a minor component ($\leq$3.5 mol%) that is considered as insignificant in regards to the bulk composition of the hydrothermal fluids (Azbej et al., 2007). Therefore, the salinities at Dabu were calculated using ice-melting temperatures for aqueous FIs (V-type and L-type) (Bodnar, 1993) and equation given by Sterner et al. (1988) for halite daughter mineral-bearing FIs (S-type), assuming a simple H_2O–NaCl system. Salinity is reported as weight percent NaCl equivalent (wt.% NaCl equiv.). Microthermometric results of 329 quartz-hosted FIs of different stages are presented in Table 1, Fig. 9 and Fig. 10.

5.3.1. Stage I

FIs in this stage are predominated by V-type, followed by L-type and S-type, among which the V-type and L-type FIs mostly homogenize at 272–475 °C, with ice-melting temperatures of –21.2 to –1.2 °C. In detail, V-type FIs have homogenization temperatures of 303–475 °C and ice-melting temperatures varying from −20.3 to −1.2 °C, corresponding to salinities of 2.1–22.6 wt% NaCl equiv. L-type FIs homogenize at 272–423 °C, with ice-melting temperatures ranging from −21.2 to −1.9 °C, which correspond to salinities from 3.2 to 23.2 wt% NaCl equiv. The S1-type FIs exhibit halite dissolution temperatures that vary from 254 to 342 °C, with calculated salinities ranging from 35.0 to 41.7 wt% NaCl equiv. The S2-type FIs exhibit halite dissolution temperatures that vary from 274 to 415 °C, with calculated salinities ranging from 36.2 to 49.1 wt% NaCl equiv.

5.3.2. Stage II

V-type and L-type FIs are both commonly present in this stage, whereas S-type FIs are rarely observed. The L-type FIs have homogenization temperatures of 244 to 390 °C, and final ice-melting temperatures of −17.7 to −0.6 °C that indicate salinities of 1.1 to 20.8 wt% NaCl equiv. The V-type FIs have homogenization temperatures from 293 °C to 438 °C, final ice-melting temperatures from −16.2 to −1.1 °C, and salinities from 2.0 to 9.3 wt% NaCl equiv. S1-type FIs homogenize at 275–456 °C, in which halite crystals dissolved at temperatures of 161–456 °C, corresponding to salinities of 30.1 to 54.0 wt% NaCl equiv. In S2-type FIs, the vapor bubbles disappeared at temperatures of 221 to 468 °C, halite crystals dissolved at temperatures of 304 to 470 °C, corresponding to salinities of 35.6 to 55.8 wt% NaCl equiv.

5.3.3. Stage III

Only L-type FIs were observed in quartz for this stage. They yield homogenization temperatures of 299–399 °C and

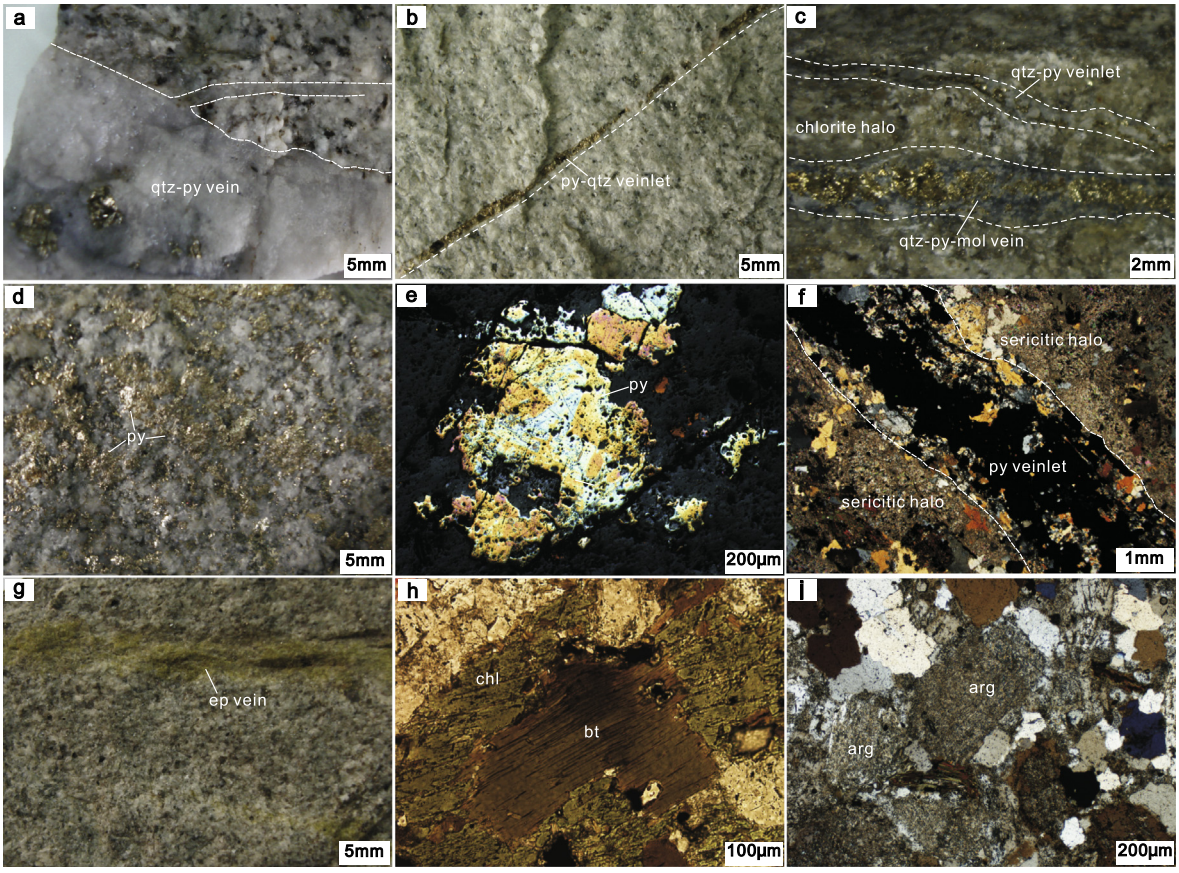

Fig. 6. Vein types, alteration and mineralization mineral assemblages of stage III at Dabu Cu-Mo deposit. (a) quartz–pyrite vein; (b) pyrite–quartz veinlet; (c) irregular quartz–pyrite veinlet and quartz–pyrite–molybdenite vein showing chlorite alteration halo along the margins; (d) medium- to fine-grained pyrite filling along the cracks; (e) subhedral to euhedral-ragged pyrite; (f) pyrite veinlet dominated by the presence of scaly-acicular and anhedral sericitic halo; (g) epidote vein; (h) fine- to medium-grained chlorite along the rims of primary biotite phenocryst; (i) argillic alteration characterized by selective pervasive replacement of feldspar by clay minerals. Abbreviations: qtz–quartz, bt–biotite, py–pyrite, mol–molybdenite, chl–chlorite, ep–epidote; arg–argillic.

ice-melting temperatures of −1.7 to −14.2 °C, which correspond to salinities of 2.9–18.0 wt% NaCl equiv.

In summary, the stage I and II quartz veins of Dabu deposit contain L, V, and S-type FIs, with similar homogenization temperatures mainly between 340 °C and 400 °C, and show two high temperature fluid populations (Fig. 9a, b, c, d). Population-I is characterized by high salinity, halite-bearing S-type inclusions with homogenization temperature ranging from 274 to 486 °C and salinity varying from 30.1 to 55.8 wt% NaCl equiv. Population-II consists of low salinity, L-type and V-type inclusions with homogenization temperature ranging from 244 to 475 °C and salinity varying from 1.1 to 23.2 wt% NaCl equiv., which plots between the halite saturation curve and the critical curve of NaCl solution in the $T_{h,\ L\text{-}V}$ vs. salinity diagram (Fig. 10). On the contrary, only one fluid populations are observed in the stage III quartz veins, evidenced by high temperature, low salinity, and L-type FIs (Fig. 9e, f).

6. H-O-S-Pb isotopic results

The analytical results of oxygen and hydrogen isotopes are listed in Table 2 and plotted in Fig. 11. The measured $\delta^{18}O_{quartz}$ and δD values of ten quartz samples in different stages range from 8.2‰ to 10.6‰ and −122‰ to −87‰, respectively. The $\delta^{18}O_{H2O}$ values of ore-forming fluids are calculated using the equation of $1000\ \ln\alpha_{quartz-H2O} = 3.38 \times 10^6\ T^{-2} - 3.40$ (Clayton et al., 1972), combined with the measured $\delta^{18}O_{quartz}$ values and the corresponding FIs homogenization temperatures of the quartz samples in this study. The calculated $\delta^{18}O_{H2O}$ values of stage I veins are between 4.5‰ and 6.6‰, with measures $\delta^{18}O_{quartz}$ and δD values varying from 8.2‰ to 9.3‰ and −109‰ to −115‰, respectively. The calculated $\delta^{18}O_{H2O}$ values of stage II veins are between 4.6‰ and 7.5‰, with measures $\delta^{18}O_{quartz}$ and δD values varying from 9.2‰ to 10.5‰ and −102‰ to −122‰, respectively. The calculated $\delta^{18}O_{H2O}$ values of stage III veins are between 5.1‰ and 6.5‰, with measures $\delta^{18}O_{quartz}$ and δD values varying from 9.8‰ to 10.6‰ and −87‰ to −99‰, respectively.

The $\delta^{34}S$ values of seventeen mineral separates of chalcopyrites, molybdenite and pyrite in the Dabu deposit are summarized in Table 3 and Fig. 12. The overall S isotopic range is from −3.6‰ to −0.2‰. The chalcopyrite separates have $\delta^{34}S$ values ranging from −3.6‰ to −1.3‰ with an average of −2.3‰, whereas the pyrite samples have $\delta^{34}S$ values from −1.1‰ to −0.2‰. Two molybdenite samples have $\delta^{34}S$ values of −0.7‰ and −1.0‰, respectively. In general, the $\delta^{34}S$ values of sulfides display a gradually increasing trend from stage I (−3.6‰ to −0.7‰) to stage II (−2.6‰ to −0.2‰).

The lead isotope data of sulfide minerals are listed in Table 4 and shown in Fig. 13. Six pyrite samples at Dabu give uniform lead isotope ratios of $^{206}Pb/^{204}Pb = 18.268$ to 18.488, $^{207}Pb/^{204}Pb = 15.604$ to 15.673, and $^{208}Pb/^{204}Pb = 38.520$ to 38.836. One molybdenite sample has a $^{206}Pb/^{204}Pb$ ratio of 18.260, a $^{207}Pb/^{204}Pb$ ratio of 15.582, and a $^{208}Pb/^{204}Pb$ ratio of 38.472.

7. Discussion

7.1. Nature of ore-forming fluid and metal source

Fluid inclusions provide a record of ore-forming fluid systems, and they provide insights into the nature and genesis of the

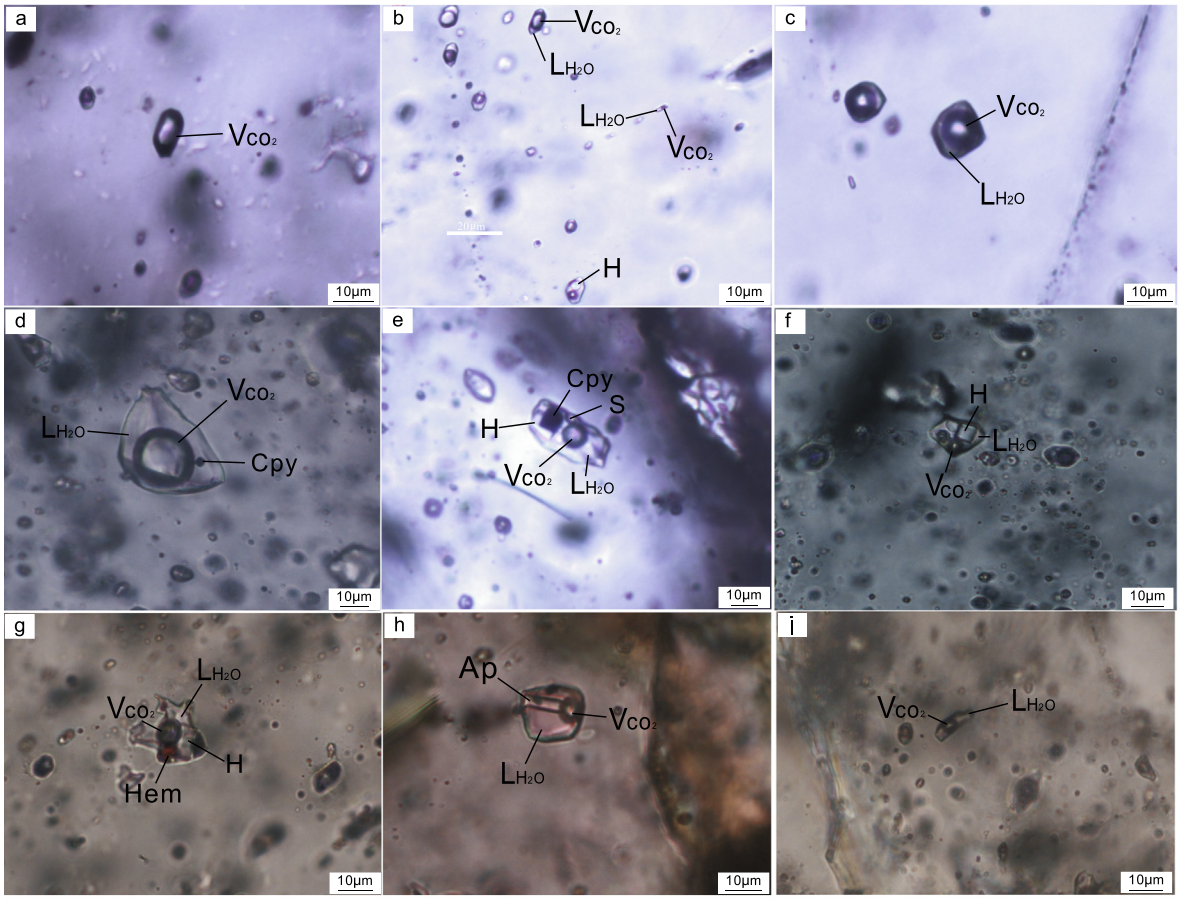

Fig. 7. Photomicrographs showing the types and characteristic features of fluid inclusions (FIs) at Dabu deposit. (a) Monophase vapor inclusion; (b) Coexistence of halite-bearing S-type, vapor-rich V-type, and liquid-rich L-type FIs; (c) Vapor-rich two-phase aqueous inclusion; (d) S-type inclusion containing opaque chalcopyrite; (e) Halite-bearing S-type inclusion with opaque chalcopyrite and sulfur; (f) Halite-bearing S-type inclusion; (g) Halite and hematite-bearing S-type inclusion; (h) Apatite-bearing S-type inclusion without halite; (i) Liquid-rich two-phase aqueous inclusion.

original fluids (Roedder, 1984; Ulrich et al., 1999; Pirajno, 2009). Compared to the early stage I and II, quartz in the late ore stage III contains only L-type FIs, which have homogenization temperatures of 299 to 399 °C close to those of stage I and II, but lower salinities ranging from 2.9 to 18.0 wt% NaCl equiv. (Fig. 9e, f). The ore-forming fluids are not characterized by a decreasing trend in temperature, but a distinct change in salinity during the evolution from stage I to stage III, indicating a similar ore fluid source for both vein types and an insignificant control of temperature on the mineralization in the Dabu deposit. The Laser Raman spectroscopy and micropetrography of FIs revealed the presence of CO_2 as the vapor phase, H_2O as the fluid phase, as well as some daughter minerals such as halite, sylvite, apatite, chalcopyrite and hematite (Fig. 8), which were supported by the petrographic observation (Fig. 7). Thus, the ore-forming fluids of Dabu deposit are characterized by high temperature, high salinity and high oxygen fugacity and belong to halite- and rare CO_2-bearing fluids of a H_2O–NaCl system, in which the existence of CO_2 can be ignored. Fluid boiling in the Dabu deposit is supported by the coexistence of S1-type, vapor-rich V-type and liquid-rich L-type FIs in quartz of stage I and II (Fig. 7b) with similar homogenization temperatures but contrasting salinities of these FIs (Fig. 9; Fig. 10). In the ore stage I and II, fluid boiling events resulted from rapid decrease of pressure, causing vapor-rich and liquid-rich phase separation from supercritical fluid and inhomogeneous entrapment of halite-saturated hydrothermal brine, which would led to a significant change in salinity and metal precipitation at Dabu due to sulfide saturated in solutions.

The hydrothermal quartz in veins or veinlets from Dabu deposit display highly clustered $\delta^{18}O_{H2O}$ values of 4.4‰ to 7.5‰, similar to primary magmatic water (Taylor, 1974), indicative of a single magmatic origin rather than multiple sources of oxygen (Fig. 11). Quartz samples from both stage I and II show slightly lower δD values (−122‰ to −102‰) than those from stage III (−99‰ to −87‰), all of which are significantly depleted when compared with typical magmatic water (Fig. 11). The low δD values of Dabu deposit can be explained by the magma degassing process (Rye, 1993), which has also been observed in porphyry deposits elsewhere, including Wunugetushan porphyry Cu-Mo deposit (Tan et al., 2013) and Chalukou porphyry Mo deposit (Liu et al., 2014b). In a δD vs. $\delta^{18}O$ diagram (Fig. 11), all of the H–O isotopic data of quartz from stage I to III fall in the field below the primary magmatic water and overlapped with the plotted area of quartz samples from Qulong porphyry Cu–Mo deposit in the GPCB (Yang, 2008), indicative of fluid derivation from degassed magmatic water, with no contributions from basinal or meteoric water.

The $\delta^{34}S_{V\text{-}CDT}$ values of sulfides in the Dabu deposit range from −3.6‰ to −0.2‰ (average −1.6‰, n = 17), within the $\delta^{34}S$ variation of sulfides from the majority of magmatic hydrothermal deposits (−3 to +1‰; Hoefs, 2009). In general, the S isotopic compositions of the chalcopyrites, molybdenite and pyrite in this study together with data from previous studies (Qu et al., 2007) of the Dabu deposit display a normal distribution with a narrow range (−3.6‰ to 1.2‰, average −1.3‰, n = 21) in a $\delta^{34}S$ histogram (Fig. 12a). These values are analogous to $\delta^{34}S$ values of whole rock Miocene ore-related high Sr/Y intrusions at the Dabu deposit

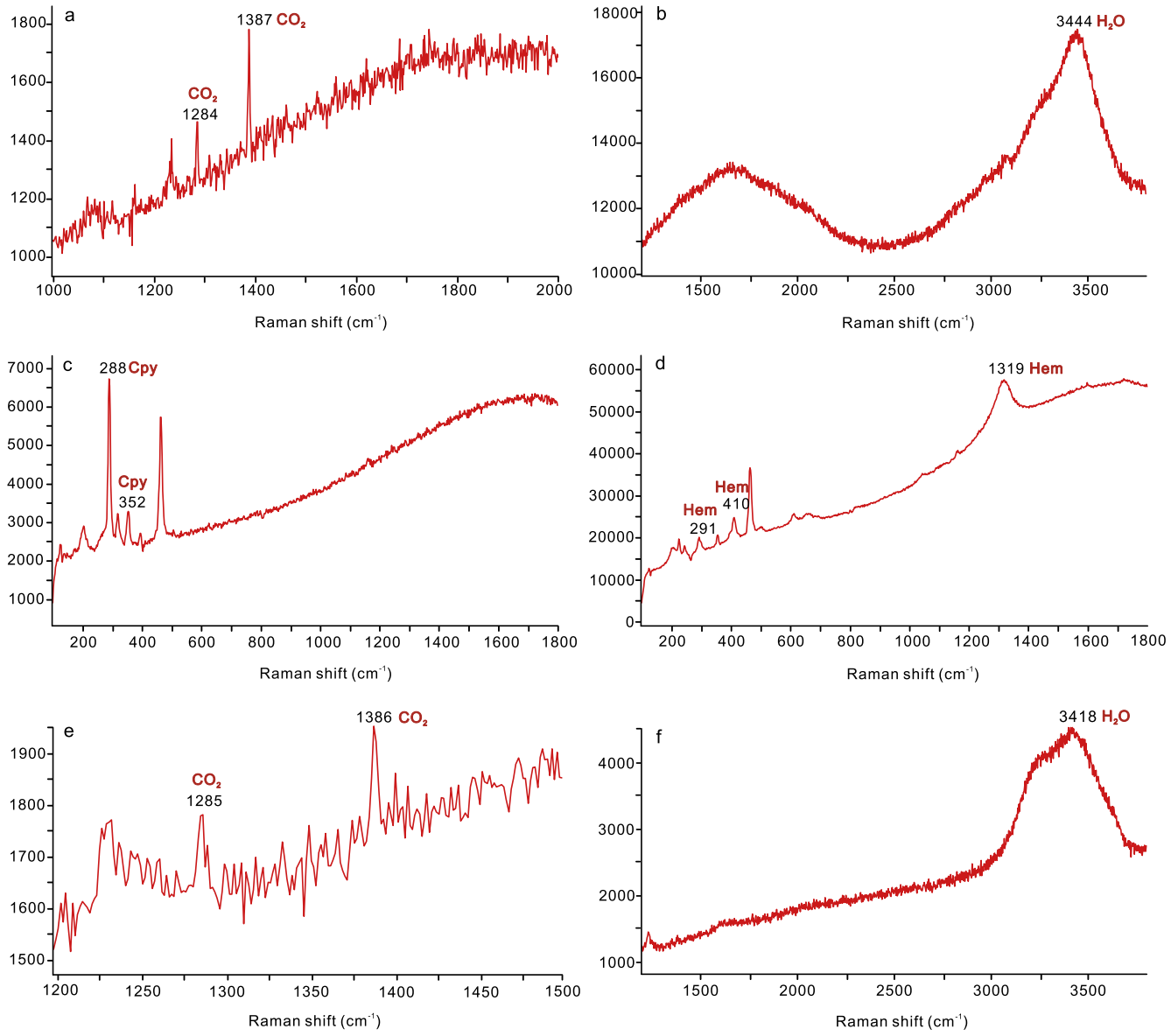

Fig. 8. Representative Laser Raman spectra of fluid inclusions in the Dabu Cu–Mo deposit. (a) CO_2 spectra of vapor phase in the V-type inclusions of stage I; (b) H_2O spectra of liquid phase in the V-type inclusions of stage II; (c) daughter chalcopyrite in the S-type inclusions of stage II; (d) daughter hematite in the S-type inclusions of stage II; (e) CO_2 spectra of vapor phase in the L-type inclusions of stage III; (b) H_2O spectra of liquid phase in the L-type inclusions of stage III.

Table 1
Summary of microthermometric data of fluid inclusions from hydrothermal quartz in the Dabu deposit.

Stage	Vein type	FIs type	N	Size (μm)	$T_{m,\ ice}$ (°C)	$T_{h,\ total}$ (°C)	Salinity (wt.%NaCl equiv)
I	quartz–K-feldspar (biotite)±chalcopyrite ± pyrite veins	V	61	5–30	−20.3 to −1.2	303–475	2.1–22.6
		L	26	5–30	−21.2 to −1.9	272–423	3.2–23.2
		S	16	7–24		274–469	35.0–49.1
II	quartz–molybdenite ± pyrite ± chalcopyrite veins	V	83	4–27	−16.2 to −1.1	293–438	2.0–9.3
		L	76	2–24	−17.7 to −0.6	244–390	1.1–20.8
		S	22	4–20		275–486	30.1–55.8
III	quartz–pyrite ± molybdenite veins	L	45	3–24	−14.2 to −1.7	299–399	2.9–18.0

(−0.6‰ to 0.8‰; Fig. 12a; Qu et al., 2007), indicative of a genetic link between sulfide origin and Miocene intrusions. In addition, all the S isotopic data of Dabu deposit show a gradually decreasing trend of $\delta^{34}S$ (Mol) > $\delta^{34}S$ (Py) > $\delta^{34}S$ (Cpy) (Fig. 12a), similar to Qulong porphyry Cu-Mo deposit in Tibet (Fig. 12b; She et al., 2005; Meng et al., 2006) and Butte porphyry Cu-Mo deposit in Montana (Lange and Cheney, 1971), reflecting isotope equilibrium during the evolution of the mineralization (Ohmoto, 1972). Moreover, the results of Dabu deposit is consistent with sulfur data of other porphyry deposits in the GPCB (Fig. 12c; She et al., 2005; Meng et al., 2006; Qu et al., 2007; Wang et al., 2015b; Zhao et al., 2015) including Bangpu (−2.3‰ to +0.7‰), Qulong (−2.7‰ to + 1.1‰), Tinggong (−1.7‰ to +2.1‰), and Chongjiang (−5.1‰ to +0.9‰), all of which are close to the primitive mantle range

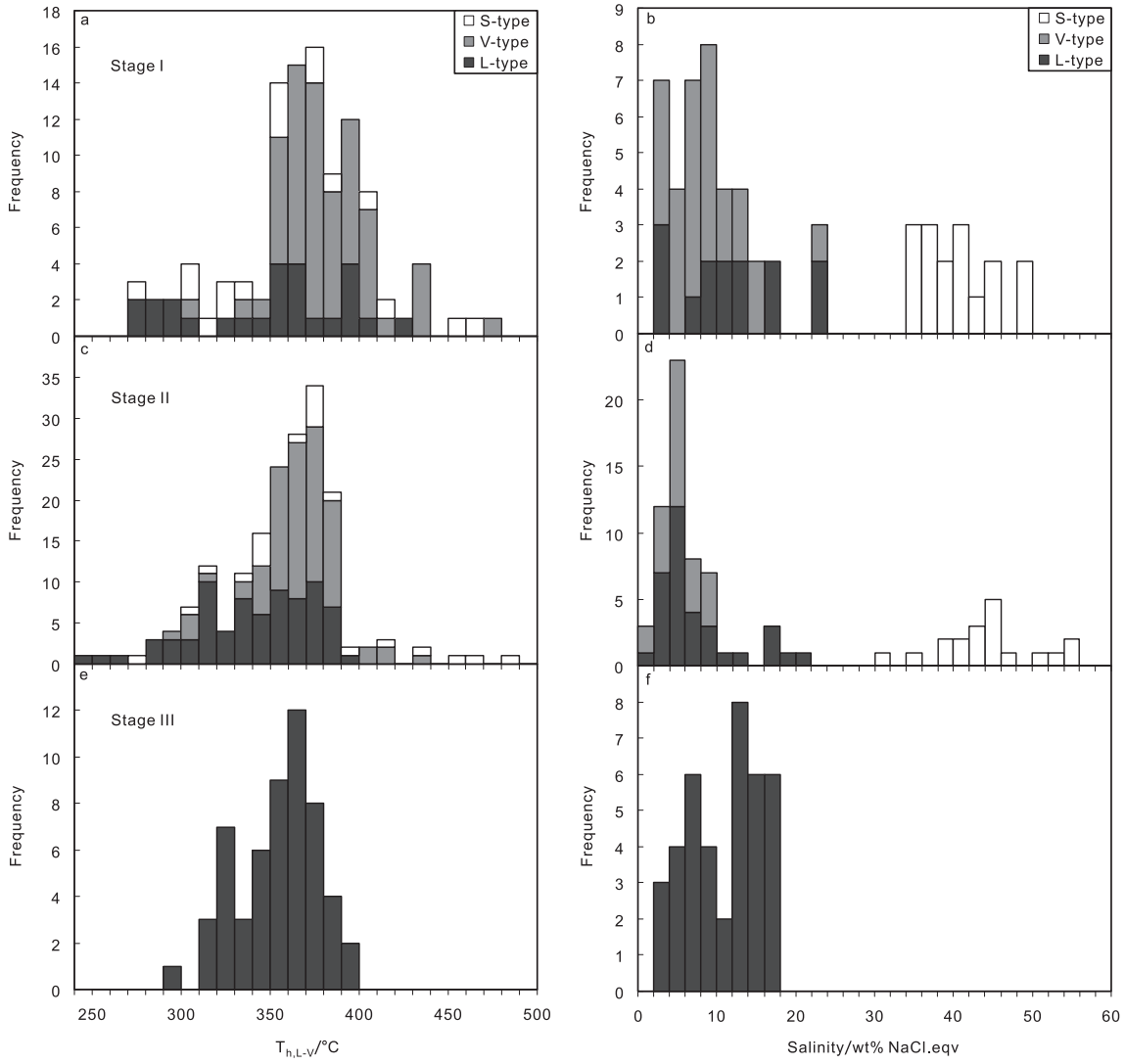

Fig. 9. Histograms of homogenization temperature and salinity of fluid inclusions in different stage quartz at Dabu Cu–Mo deposit. V-type–Vapor-rich two-phase FIs, L-type–Liquid-rich two-phase FIs, S-type–Solid bearing multi-phase FIs.

(+0.5‰; Chaussidon et al., 1989), indicating contribution from the mantle to the ore-forming fluids. On the contrary, the $\delta^{34}S$ values of sulfides from Sharang porphyry Mo deposit are relatively higher than those of Dabu deposit and beyond the range of mantle, which may suggest more contributions from mature continental crustal materials (Sun et al., 2017). We therefore propose that the sulfur sources of the Dabu deposit were undiversified and deeply sourced magmatic sulfur (Ohmoto and Rye, 1979) potentially linked with Miocene granitoid intrusions.

The Pb isotopic data of molybdenite and pyrite from Dabu deposit have relatively uniform ranges, with $^{206}Pb/^{204}Pb$ ratios of 18.260 to 18.488, $^{207}Pb/^{204}Pb$ ratios of 15.582 to 15.673, and $^{208}Pb/^{204}Pb$ ratios of 38.472 to 38.836. In the $^{206}Pb/^{204}Pb$ vs. $^{207}Pb/^{204}Pb$ diagram (Zartman and Doe, 1981), most of the data points for sulfides fall within the field between the upper crust and orogenic evolution curves, partly plotting in the area below the orogenic evolution curve (Fig. 13a). Similarly, all the data points for sulfide minerals are located in the domain between the orogenic belt and the lower crust evolution line in the $^{206}Pb/^{204}Pb$ vs. $^{207}Pb/^{204}Pb$ diagram (Fig. 13b; Zartman and Doe, 1981). It is worth noting that the Pb isotopes of sulfide minerals from Dabu deposit share similar characteristics with those of ore samples in Qulong and Tinggong porphyry deposits in the GPCB (Fig. 13), indicating that Pb was mostly derived from a deep-seated magma. Moreover, the sulfides and host intrusions in the Dabu, Qulong and Tinggong show indistinguishable lead isotopic compositions (Fig. 13). The analogous lead isotopes imply that the ores and ore-related intrusions have a common lead source region, and indicate that the Miocene granitic magmatism is largely responsible for the Cu and Mo mineralization in the Dabu deposit as well as other porphyry deposits in GPCB.

In summary, based on the above mentioned characteristics of FIs and H–O–S–Pb isotopes, it is concluded that Dabu deposit formed in a H_2O–NaCl magmatic–hydrothermal system with high temperature, high salinity and high oxygen fugacity, and boiling is the major factor for metal precipitation. The ore-forming fluids and materials show evidence of a magmatic origin linked to the Miocene high Sr/Y intrusions in the GPCB, similar to other porphyry deposits in this belt.

7.2. Comparison with other porphyry deposits

7.2.1. Pressure estimation and mineralization depth

The entrapping pressure of fluid can be estimated through FIs formed in an immiscible or boiling system (i.e., coeval liquid and/or saline- and vapor-rich inclusions with identical

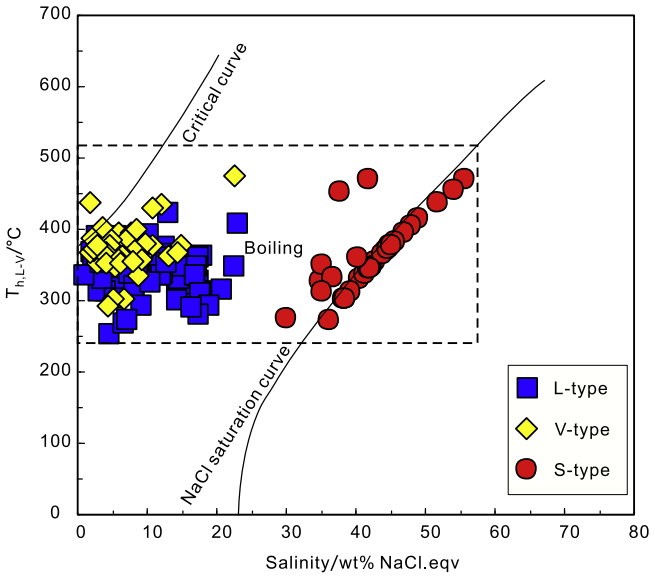

Fig. 10. Homogenization temperature vs. salinity plot for different types of fluid inclusions data from the Dabu Cu–Mo deposit relative to the NaCl saturation curve and critical curve (Ahmad and Rose, 1980). V-type–Vapor-rich two-phase FIs, L-type–Liquid-rich two-phase FIs, S-type–Solid bearing multi-phase FIs.

homogenization temperatures) (Roedder and Bodnar, 1980; Shepherd et al., 1985; Brown and Hagemann, 1995; Ulrich et al., 2001). Petrographic and microthermometric data suggest that the majority of the saline-bearing S1-type, vapor-rich V-type and liquid-rich L-type FIs in stage I (A-type vein) quartz–K-feldspar (biotite) ± chalcopyrite ± pyrite veinlets or veins were formed through fluid boiling. Therefore, we can estimate the exact trapping pressures of stage I FIs in the Dabu deposit. The porphyry ore-forming system characterized by pulsating hydraulic breakage and healing caused by fluid immiscible/boiling and precipitation, can be interpreted as a state that frequently alternates between supra-lithostatic to lithostatic and hydrostatic pressures (Sillitoe, 2010). Thus, the lowest trapping pressure of the FIs represents the hydrostatic system, whereas the highest trapping pressure reflects the lithostatic to supralithostatic system. Given that the majority of boiling FIs were trapped at lower temperatures (approximately $\leq$ 450 °C; Fig. 14), we infer all the inclusions in early stage I A-type veins were formed in a brittle environment under hydrostatic conditions, assuming a fluid density near 1 g/cm^3.

When assuming a simple NaCl–H_2O system, the formula given by Driesner and Heinrich (2007) can be used to estimate trapping pressure. For coexisting L-,V- and S1-type FIs in stage I, trapping pressures are mostly between 100 and 400 bars, and corresponds to a depth of 1.0 to 4.1 km (hydrostatic pressure and a rock density of 1.0 g/cm^3) (Fig. 14a). For S2-type fluid inclusions, only minimum trapping pressures could be calculated via using the empirical equation proposed by Becker et al. (2008). The minimum trapping pressures are heterogeneous and range mostly from 500 to 2300 bars (Fig. 14b), significantly higher than that of S1-type inclusions. The S2-type FIs which homogenize by halite dissolution can either be caused by direct exsolution from parent magma, or formed through a process of postentrapment modification, or trapped after being overpressured (Shu et al., 2013 and references therein). In view of the coexisting S1- and S2- type FIs, and analogous homogenization temperatures of low-salinity inclusions and brine inclusions in stage I of Dabu deposit, we thus proposed that the S2-type FIs were generated from the post-entrapment modification of S1-ype FIs because of H_2O loss (Audétat and Günther, 1999; Klemm et al., 2008).

Besides, the trapping pressures of stage I FIs can also be estimated using the homogenization temperatures and salinities of the boiling FIs on the basis of microthermometric observations of inclusions in which vapor is the last phase to homogenize, following the methods of Urusova (1975), Haas (1976), and Bodnar et al. (1985) when assuming a simple NaCl–H_2O system. For the Dabu deposit, the boiling FIs in A-type veins have homogenization temperatures of 272–434 °C and salinities between 2.6 and 40.4 wt% NaCl equiv., corresponding to entrapment pressures of 5–33 MPa and mineralization depths of 0.5–3.4 km assuming a hydrostatic condition (Fig. 15).

Previous studies demonstrated that the ore-related Miocene intrusions from Qulong (giant), Zhunuo (large) and Dabu (small) porphyry deposits have comparable geochemical features, such as high Sr/Y, La/Yb, V/Sc ratios as well as high zircon Ce^{4+}/Ce^{3+} ratios (Fig. 16; Wang et al., 2006; Yang, 2008; Hu et al., 2015; Lu et al., 2016; Wu et al., 2016; Zeng et al., 2017), indicative of indistinguishable magmatic oxygen fugacity and water content between each deposit (Loucks, 2014; Lu et al., 2015). Thus, it seems likely that shallow hydrothermal process is the main controls on the formation of Qulong, Dabu, and Zhunuo deposits with different grade and tonnage, rather than magmatism occurred at the deep magma chamber. As shown in Fig. 15, boiling FIs in the A-type veins of Qulong (Xiao et al., 2012) and Zhunuo (Li et al., 2015) deposits exhibiting final homogenization by vapor disappearance were also plotted for comparison. The boiling FIs in A-type veins from Zhunuo deposit have homogenization temperatures of 230–415 °C and salinities between 6.0 and 45.3 wt% NaCl equiv., corresponding to entrapment pressures of 2–29 MPa (Fig. 15; Li et al., 2015). For Qulong deposit, the boiling FIs in A-type veins have homogenization temperatures of ca. 390–450 °C and salinities between ca. 1.9 and 49.0 wt% NaCl equiv., corresponding to entrapment pressures of 16–42 Mpa (Fig. 15; Xiao et al., 2012). The estimated mineralization depths of Qulong, Dabu and Zhunuo deposits are 1.6–4.3 km, 0.5–3.4 km and 0.2–3.0 km, respectively. This estimate shows that the mineralization depths of porphyry deposits in the GPCB gradually decreased from eastern to western segments.

Table 2
Hydrogen and oxygen isotopes for quartz in the Dabu deposit.

Stage	Sample No.	Mineral	Th (°C)	$\delta^{18}O_{quartz}$	$\delta^{18}O_{H2O}$	δD_{H2O}
I	ZK0004-120	quartz	469	9.3	6.6	−109
I	ZK0004-100	quartz	415	8.2	4.5	−115
II	DB11-48	quartz	378	10.3	5.7	−113
II	ZK0004-300	quartz	437	9.3	6.0	−117
II	DB11-61	quartz	456	10.5	7.5	−122
II	ZK0004-68	quartz	378	9.2	4.6	−113
II	DB11-43	quartz	364	9.3	4.4	−102
III	DB11-65	quartz	399	10.6	6.5	−99
III	DB11-9-2	quartz	378	10.3	5.7	−87
III	DB11-46	quartz	374	9.8	5.1	−97

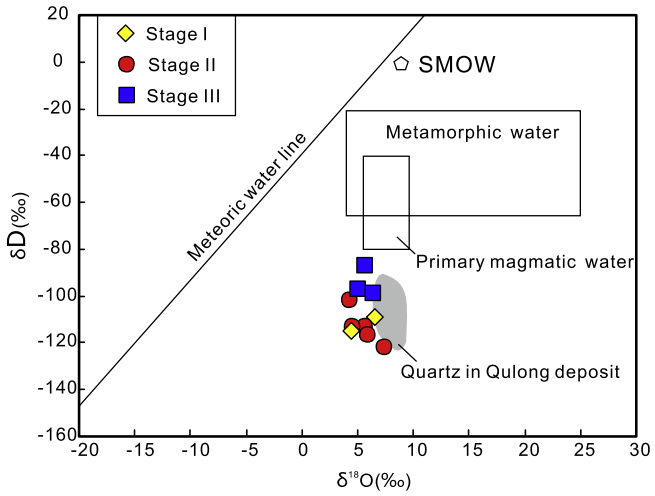

Fig. 11. δD and $\delta^{18}O$ values of the ore fluids in the Dabu Cu–Mo deposit. The common metamorphic water field, the magmatic water field, SMOW, and the meteoric water line are from Taylor (1974). The field of quartz in Qulong deposit is from Yang (2008). SMOW = standard mean ocean water.

The formation of the giant-sized Qulong deposit with >10 Mt Cu could be the result of deep processes. As illustrated through experiments that the solubility of H_2O and most volatiles in melts decrease when pressure decrease (Cline, 1995; De Vivo et al., 2005), therefore, the exsolution of aqueous fluids with large fraction of water and chlorine in deeper levels with higher pressures can extract more copper from melts, whereas the extracted copper is smaller in shallow systems due to less dissolved water and chlorine in the melts (Cline and Bodnar, 1991). It is concluded that the total amount of precipitated metal at shallow levels such as Zhunuo are relatively less than those at deeper levels such as Qulong if the initial melts are similar. However, the formation of small-sized Dabu deposit can be explained by the single magmatic-hydrothermal activity related to Miocene monzogranite porphyry during mineralization (Fig. 2), whereas multiphase magmatic-hydrothermal events have been found in both the Zhunuo and Qulong mining areas which may have provided additional S, metal, as well as thermal energy, leading to the formation of relatively larger deposits (Yang, 2008; Zheng et al., 2012b; Li et al., 2015).

Murakami et al. (2010) systematically estimated the formation depth of 50 major porphyry-style Cu–Au ± Mo deposits worldwide by using published geological information as well as fluid inclusion microthermometry data. They found general correlations of Cu/Au ratio, and individual metal grades of Cu, Mo, Au with depth and pressure of ore formation, and suggest a combination of magma source characteristics and the subsequent physical–chemical evolution of cooling ore-forming hydrothermal fluids controls on the metal type and grade variations of porphyry deposits (Murakami et al., 2010). To better understand the diversity of porphyry Cu-Mo mineralization in GPCB, a simple comparison of mineralization depth variations estimated through fluid inclusion data of other porphyry deposits formed in different geodynamic setting has been undertaken. As shown in Fig. 17, the mineralization depths of porphyry Cu-Mo deposits in GPCB are less than 4 km, similar to those of most porphyry Cu ± Au deposits in the Circum-Pacific metallogenic belt (CPMB) such as Bingham deposit in Utah (Redmond et al., 2004), both of which are restricted with the range of mineralization depths of approximately 1–5 km below the paleosurface for most porphyry ore deposits (Pirajno, 2009). In general, the porphyry Cu deposits in CPMB were formed at relatively greater depth than porphyry Cu-Au deposits in this belt, whereas the mineralization of porphyry Cu-Mo deposits in CPMB occurred at depths of more than 4 km such as La Verde deposit in Mexico (Fig. 17). Particularly, the Butte porphyry Cu-Mo deposit in Montana is estimated to have formed at 6 to 9 km, in contrast to ~3 km for most other porphyry-type deposits (Rusk et al., 2004). This unusually great depth can be interpreted by nearly constant magmatic fluids expelled at pressures and temperatures above the immiscibility gap in the CO_2–H_2O–NaCl system and supercritical fluids trapped before fluid unmixing, which were repeatedly or continuously recharged by external volatile sources from deep magma chamber to account for the formation of gigantic porphyry deposit at Butte (Rusk et al., 2004, 2008). For porphyry Mo deposits in the Dabie-Qinling collisional orogens (DQCO) such as Donggou and Yaochong deposits, their mineralization depths are also higher than those of porphyry Cu-Mo deposits in GPCB (Fig. 17; Wang et al., 2014d; Yang et al., 2015b). We therefore conclude that variations in mineralization depth have a significant control on the formation of porphyry deposits with different metal types (e.g., porphyry Cu, Mo, Cu-Au), probably owing to the influence of emplacement depth of source magma body on the availability of metals and the salinity of the exsolved fluid (Cline and Bodnar,1991; Murakami et al., 2010; Richards, 2015).

7.2.2. Sulfur and oxygen isotopic compositions

Sulfur and oxygen isotopic studies can provide useful insights into the ore-fluid sources of porphyry deposits. The data of S and

Table 3
Sulfur isotopic data of sulfides from the Dabu deposit.

Sample No.	Mineral	Stage	Occurrence of sulfide	$\delta^{34}S_{V\text{-}CDT}$ (‰)
DB303-238	Pyrite	I	Star-like distributed	−0.9
DB303-238	Chalcopyrite	I	Along fracture	−3.6
DB0003-350	Pyrite	I	Star-like distributed	−1.1
DB0003-350	Chalcopyrite	I	Along fracture	−1.3
DB11-53	Pyrite	I	Disseminated	−0.7
DB11-53	Chalcopyrite	I	Disseminated	−2.7
DB302-334	Chalcopyrite	I	Disseminated	−3.2
DB302-483	Chalcopyrite	I	Along fracture	−2.4
DB11-9	Molybdenite	II	Qtz-mol-py vein	−1
DB11-9	Pyrite	II	Qtz-mol-py vein	−0.7
DB11-56	Molybdenite	II	Qtz-mol-py vein	−0.7
DB302-63	Pyrite	II	Star-like distributed	−0.2
DB302-63	Chalcopyrite	II	Along fracture	−1.8
DB303-206	Chalcopyrite	II	Qtz-cpy-ser vein	−1.3
DB302-119	Chalcopyrite	II	Along fracture	−2.6
DB003-263	Chalcopyrite	II	Along fracture	−2
DB11-61	Pyrite	III	Qtz-py-mol vein	−0.9

Abbreviations: qtz–quartz, ser–sericite, py–pyrite, cpy–chalcopyrite, mol–molybdenite.

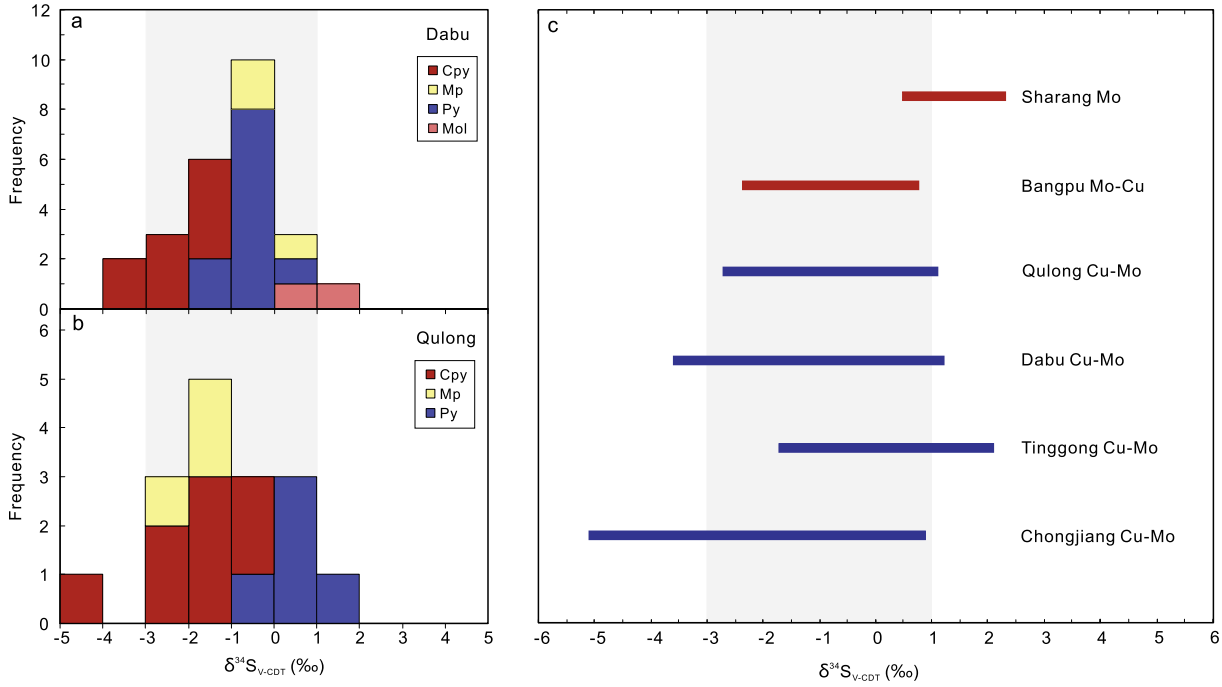

Fig. 12. Frequency histogram plots of $\delta^{34}S$ values for sulfide minerals from the Dabu (a) and Qulong (b) Cu–Mo deposits. $\delta^{34}S$ values for whole rock Miocene porphyry in the Dabu and Qulong are also shown for comparison (Meng et al., 2006; Qu et al., 2007). (c) Comparison of the Dabu deposit with other porphyry deposits in the Gangdese porphyry copper belt (She et al., 2005; Meng et al., 2006; Qu et al., 2007; Wang et al., 2015 b; Zhao et al., 2015; Sun et al., 2017). The $\delta^{34}S$ value range for magmatic hydrothermal deposits (shaded area, −3 to +1‰) is from Hoefs (2009). Abbreviations: Py–pyrite, Cpy–chalcopyrite, Mol–molybdenite, Mp–Miocene porphyry.

Table 4
Lead isotopic compositions of sulfides from the Dabu deposit.

Sample No.	Mineral	$^{206}Pb/^{204}Pb$	2σ	$^{208}Pb/^{204}Pb$	2σ	$^{207}Pb/^{204}Pb$	2σ
DB11-56	Molybdenite	18.260	0.003	38.472	0.009	15.582	0.003
DB11-59	Pyrite	18.451	0.003	38.666	0.007	15.627	0.003
DB11-9	Pyrite	18.428	0.003	38.645	0.007	15.629	0.003
DB11-61	Pyrite	18.389	0.003	38.679	0.005	15.661	0.002
DB-10	Pyrite	18.488	0.004	38.836	0.008	15.673	0.003
DB11-53	Pyrite	18.268	0.003	38.520	0.007	15.604	0.003
DB11-22	Pyrite	18.350	0.002	38.700	0.004	15.648	0.002

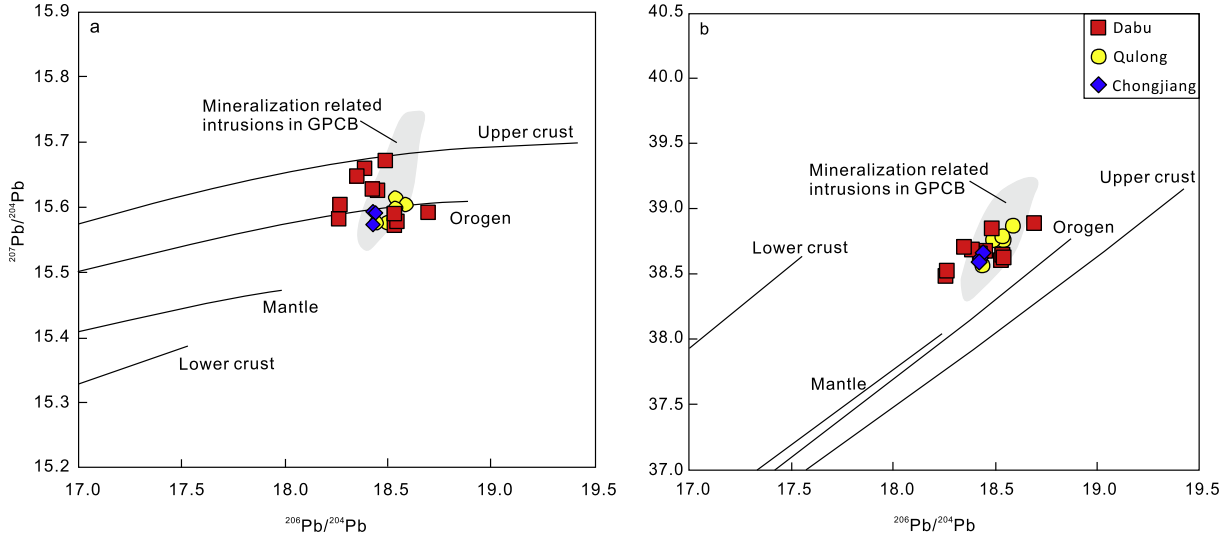

Fig. 13. Plots of $^{207}Pb/^{204}Pb$ vs. $^{206}Pb/^{204}Pb$ and $^{208}Pb/^{204}Pb$ vs. $^{206}Pb/^{204}Pb$ for sulfide minerals from the Dabu Cu–Mo deposit. Data of sulfides in the Qulong and Chongjiang deposits and area of mineralization related intrusions in GPCB are from Meng et al. (2006) and Qu et al. (2007). The basemap is from Zartman and Doe (1981).

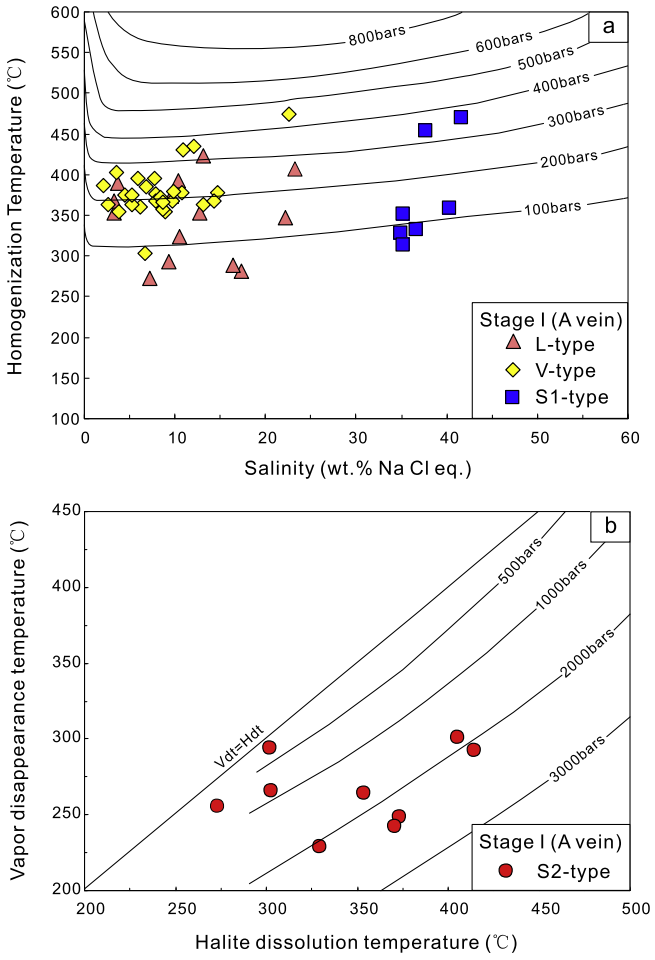

Fig. 14. Pressure estimation for fluid inclusions at stage I. a. L-, S1-, and V-type inclusions at stage I were trapped under boiling conditions, thus the estimated pressures can represent the actual trapping pressures. Isobars were calculated from the equations of Driesner and Heinrich (2007). b. S2-type inclusions at stage I were homogenized by halite dissolution and therefore their estimated pressures only represent their minimum trapping pressures. Phase diagram used was from Becker et al. (2008).

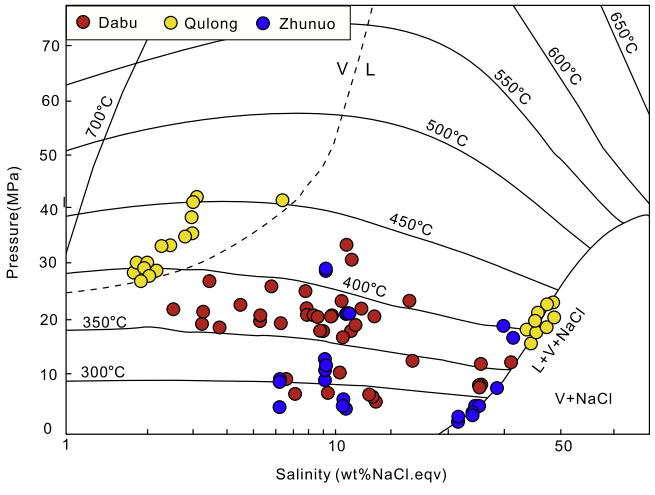

Fig. 15. Pressure estimates for boiling FIs that exhibited final homogenization by vapor disappearance (after Bouzari and Clark, 2006). The data of boiling FIs in early A-type veins from Qulong and Zhunuo deposits are also plotted here for comparison (Xiao et al., 2012; Li et al., 2015).

O isotopes from selected porphyry deposits are summarized in Fig. 18 and Fig. 19. The $\delta^{34}S$ values of sulfides from porphyry Cu-Mo deposits in the GPCB are typically around 0‰, similar to those of major porphyry Cu ± Au ± Mo deposits in the CPMB with relatively negative $\delta^{34}S$ values, although parts of which have positive $\delta^{34}S$ values such as Butte porphyry Cu-Mo deposit in Montana and Dizon porphyry Cu-Au deposit in Philippines (Fig. 18; Field et al., 2005; Imai, 2005). On the contrary, porphyry Mo deposits in the DQCO have sulfides with distinctly positive $\delta^{34}S$ values ranging from 0‰ to 10‰, which can be attributed to variations in the bulk sulfur isotopic composition of the crust-derived magma, to some degree, contributed by sulfur from wall-rock assimilation (Fig. 18). Similarly, the calculated $\delta^{18}O_{H2O}$ values through quartz samples from porphyry deposits in GPCB and CPMB are in narrow variations and higher than those of porphyry Mo deposits in the DQCO that are in relatively wide ranges reflecting the input of the meteoric water (Fig. 19). It is likely that the ore-forming fluid compositions of porphyry Cu-Mo deposits in GPCB are similar to porphyry Cu ± Au ± Mo deposits in CPMB, but differ from porphyry Mo deposits in DQCO.

7.3. Ore genesis of post-collisional porphyry Cu deposit

The genesis of post-collisional porphyry Cu deposits still remains controversial. A variety of models have been proposed, including melting of the residual downgoing slab (Qu et al., 2004; Omrani et al., 2008; Mao et al., 2014), partial melting of orogenic arc lower crust (Shafiei et al., 2009; Li et al., 2011b) or thickened mafic lower crust (Hou et al., 2011). Recently, Lee et al. (2012b) proposed that remelting of Cu-rich cumulates in the deep roots of arcs are key steps in the formation of porphyry Cu deposits, which emphasized magmatism-related thickness and maturity of continental arcs have controlled the concentration of Cu in the resulting magma, rather than sourcing any Cu from the mantle or subducting slab (Chiaradia, 2013; Lee, 2013). Similarly, Hou et al. (2015b) studied Jurassic subduction-related Cu–Au and Miocene collision-related Cu–Mo porphyry deposits in southern Tibet, and suggested that remelting of the lower crustal sulfide-bearing Cu-rich Jurassic cumulates, triggered by Cenozoic crustal thickening and/or subsequent slab break-off, led to the generation of giant Miocene porphyry Cu deposit. Based on the inferred high H_2O contents (>10 wt%) of ore-forming high Sr/Y porphyries in southern Tibet through a geohygrometer for granites using zircon-saturation thermometry and H_2O-dependent phase equilibria, Lu et al. (2015) proposed that these porphyries were derived from high-pressure differentiation of hydrous mafic partial melts of the mantle, rather than from the melting of a thickened mafic lower crust. On the other hand, Yang et al. (2015a) proposed that mixing of highly metasomatized lithospheric mantle derived ultrapotassic magma with adakite-like melt at lower and/or upper-crustal depths accounts for the formation of Gangdese porphyry Cu systems, during which time, elevated K_2O and exogenous water were added to magma. All these models were proposed emphasizing on the magmatic processes at deep magma chamber or near the crust–mantle boundary, but the shallow hydrothermal processes, which are also critical for porphyry-type mineralization, are poorly studied.

In volcanic arc setting, the fluids related to subduction associated porphyry Cu ± Au ± Mo deposits were mainly derived from metamorphic dehydration of subducted oceanic slab percolated by NaCl-brine or seawater (Sillitoe, 1972; Richards, 2003, 2011b), therefore resulting in the ore-forming fluid systems being rich in H_2O, Na and Cl, but poor in CO_2 (or carbonate), K and F (Chen et al., 2007, 2008; Chen and Li, 2009). CO_2-poor and NaCl-bearing inclusions are commonly present in the Circum-Pacific metallogenic belt such as the Grasberg Cu–Au deposit in Indonesia (Lu,

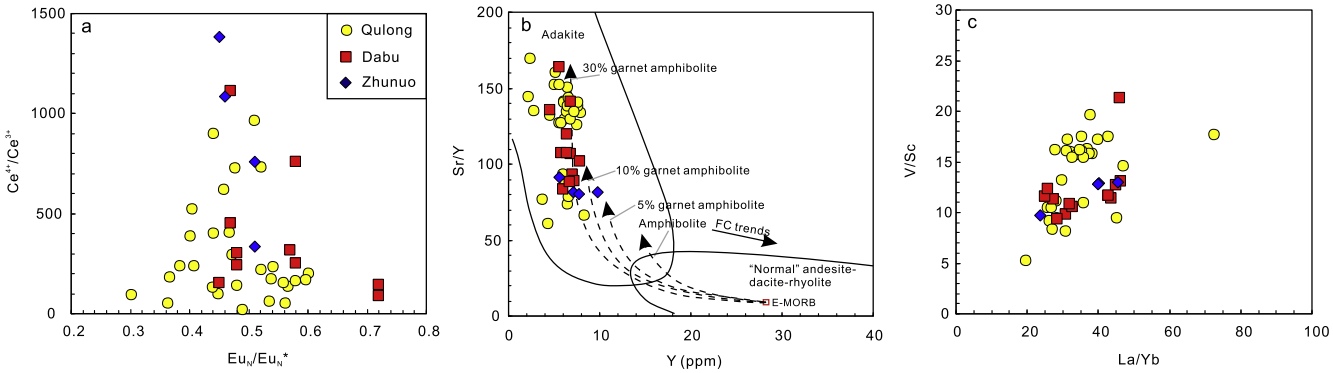

Fig. 16. Plots: (a) Zircon Ce^{4+}/Ce^{3+} vs. Eu_N/Eu_N^*; (b) Sr/Y vs. Y (Defant and Drummond, 1993); and (c) V/Sc vs. La/Yb. Published data of zircon and whole-rock trace element for ore-related Miocene intrusions in Qulong, Zhunuo and Dabu porphyry deposits are from Wang et al. (2006), Yang (2008), Hu et al. (2015), Lu et al. (2016), Wu et al. (2016) and Zeng et al. (2017). The simulated results of variable degrees of partial melting of different basaltic lower crust from Haschke et al. (2010) and Shafiei et al. (2009).

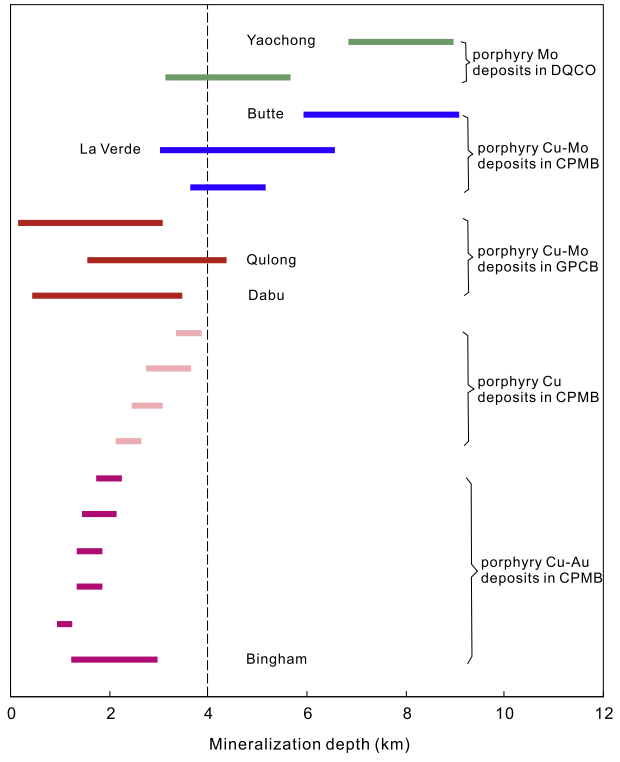

Fig. 17. Variations of mineralization depth estimated through fluid inclusion data of major porphyry deposits formed in different geodynamic setting. Data of porphyry Cu-Mo deposits in GPCB are from Xiao et al. (2012), Li et al. (2015), this study; Data of porphyry Cu ± Au ± Mo deposits in CPMB are from Redmond et al. (2004), Rusk et al. (2004), Bouzari and Clark (2006), Murakami et al. (2010). Data of porphyry Mo deposits in DQCO are from Wang et al. (2014d) and Yang et al. (2015b). Abbreviations: GPCB–Gangdese porphyry copper belt, CPMB–Circum-Pacific metallogenic belt, DQCO–Dabie-Qinling collision orogens.

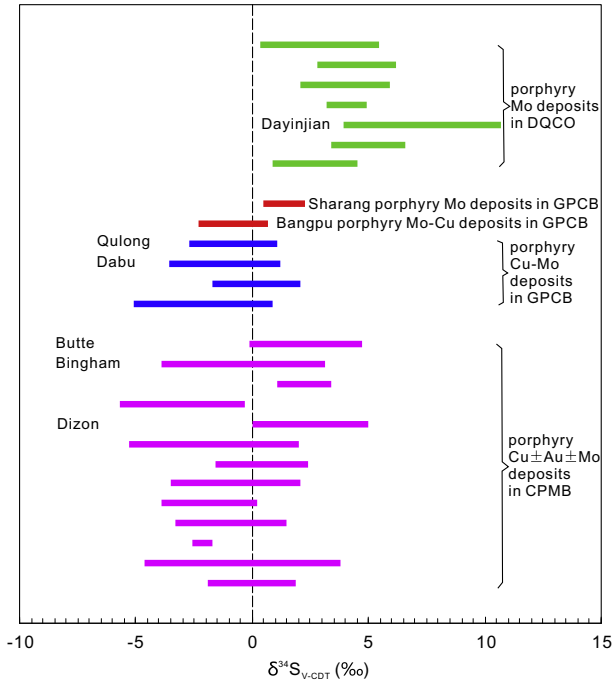

Fig. 18. Ranges of $\delta^{34}S$ values of sulfides from selected porphyry deposits formed in different geodynamic setting. Data of porphyry Cu-Mo deposits in GPCB are from She et al. (2005), Meng et al. (2006), Qu et al. (2007), Wang et al. (2015b), Zhao et al. (2015), Sun et al. (2017), this study. Data of porphyry Cu ± Au ± Mo deposits in CPMB are from Field (1966), Field and Gustafson (1976), Eastoe (1983), Kouzmanov et al. (2003), Field et al. (2005), Imai (2005), Del Rio Salas et al. (2013), Maydagán et al. (2013), Hedenquist et al. (2017). Data of porphyry Mo deposits in DQCO are from Tang (2015) and Chen et al. (2017). The abbreviations are the same as in Fig. 17.

2000). In contrast, CO_2-bearing inclusions have recently been reported in the Dabie–Qinling Mo deposits developed in syn- and post-collisional settings (Chen et al., 2017), because mineral systems in this region were sourced from the thickened continental crust that is poor in H_2O, Na and Cl, but rich in CO_2, K, and F relative to subducted oceanic crust in island or continental arcs (Tang et al., 2008, 2009; Chen and Li, 2009). It is evidenced that NaCl as a halite daughter mineral are common in the fluid inclusions of Dabu deposit, without CO_2-bearing three phases FIs, and similar phenomenons have also been reported in other Miocene porphyry Cu-Mo deposits in the GPCB (Zhang et al., 2003; Li et al., 2015; Wang et al., 2015c; Li et al., 2017). The high salinity fluid (NaCl-rich) could be generated through boiling from an intermediate-low salinity original fluid or directly exsolved from the magmas. Actually, the two end members of fluid populations (Fig. 9; 1.1–23.2% and 30.1–55.8%NaCl equiv.) observed at Dabu deposit cannot be explained by fluid boiling solely when assuming a widely believed initial fluids (~5–15% NaCl equiv.) that are lower than the upper limit (~23.2%) of Dabu low salinity ranges. Therefore, we prefer the high salinity FIs in Dabu and other deposits in GPCB to be a diagnostic indicator to reflect the features of primary magma, rather than the boiling process. The ore-forming hydrothermal fluids of post-collisional porphyry Cu-Mo deposits in GPCB of south Tibet were suggested to be enriched in NaCl, in

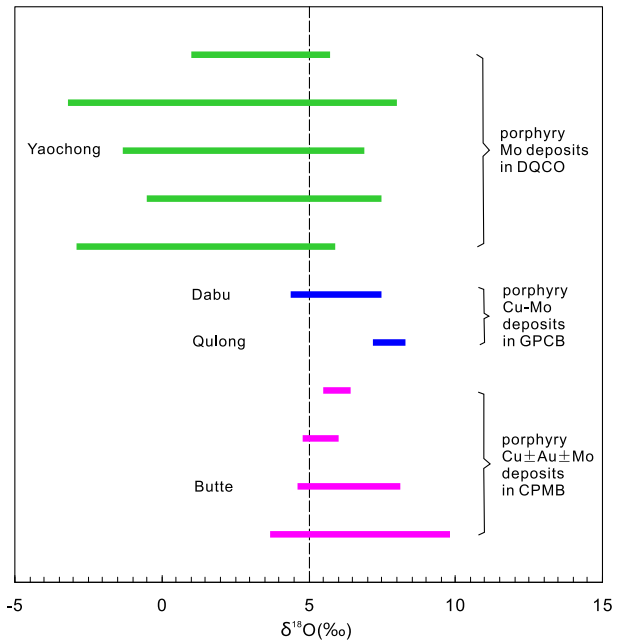

Fig. 19. Ranges of $\delta^{18}O_{H2O}$ values of quartz from selected porphyry deposits formed in different geodynamic setting. Data of porphyry Cu-Mo deposits in GPCB are from Yang (2008), this study. Data of porphyry Cu ± Au ± Mo deposits in CPMB are from Harris et al. (2005), Zhang (2000), Del Rio Salas et al. (2013), Gregory (2017). Data of porphyry Mo deposits in DQCO are from Li et al. (2014b), Wang et al. (2014d), Ni et al. (2015), Yang et al. (2013, 2015b). The abbreviations are the same as in Fig. 17.

particular the Cl^-, and poor in CO_2, comparable to those of porphyry Cu ± Au ± Mo deposits in CPMB formed in oceanic subduction-related continental or island arcs.

In view of all the characteristics claimed above, it is more likely that the mineralization depth and features of primary magma source have major controls on the metal types and ore-fluid compositions of porphyry deposits. In a deeper magmatic-hydrothermal ore-forming system (>4 km), greater confining pressure is likely to precipitate Cu ± Mo only, while sulfur-complexed Au remains dissolved and CO_2 has a higher saturation in the exsolved fluids (Brown et al., 1989; Simon et al., 2000; Murakami et al., 2010; Seo et al., 2012). Thus, porphyry Mo deposit can be formed when the primary magma originated from ancient continental crust such as Yaochong porphyry Mo deposit in Dabie continental collision orogen that is dominated by CO_2-rich and NaCl-poor ore-fluid (Fig. 17; Wang et al., 2014d). On the other hand, porphyry Cu-Mo deposit can be formed when the primary magma related to subducted oceanic slabs such as Butte porphyry Cu-Mo deposit in continental arc setting that is dominated by both CO_2- and NaCl-rich ore-fluid, in which the CO_2 probably derived from the overlying continental crust above lithospheric mantle (Fig. 17; Rusk et al., 2004, 2008; Chen and Li, 2009). Otherwise, under shallower levels of mineralization depth (<4 km), the solubility of both metals decrease rapidly and CO_2 would escape from the fluids due to their lower saturation, resulting in the precipitation of Cu, Au, Mo and the trapping of CO_2-poor fluid inclusions. For example, if the magma source originated from subducted oceanic slabs, porphyry Cu-Au mineralization could occur (approximately <2 km) such as Dizon porphyry Cu-Au deposit in island arc setting (Fig. 17; Imai, 2005). For porphyry Cu-Mo deposits in GPCB, they share analogous ore-forming conditions with porphyry Cu ± Au ± Mo deposits in CPMB, including the mineralization depth (<4 km; Fig. 17), and magmatic S (cluster 0‰; Fig. 18) and O (5‰ to 10‰; Fig. 19) isotopic compositions of ore-fluids. Although they were formed in a post-collisional setting after the collision of Indian and Asian plates, their magma sources still experienced a long-lived northward subduction of the Neo-Tethyan ocean slab (Wen et al., 2008; Chung et al., 2009; Ji et al., 2009). During such processes, the Miocene ore-related high Sr/Y intrusions would inherit previously subduction-associated arc magma features with high NaCl contents sourcing from subducting slab-derived fluid and oceanic sediments through metamorphic dehydration and metasomatism, as supported by their indistinguishable arc geochemical characteristics (Qu et al., 2004; Hou et al., 2015b; Wu et al., 2016). When the fertile magma ascends to shallow depths of 2–4 km, without shallow crustal assimilation and input of the meteoric water, the hydrothermal fluid that are CO_2-poor, halite-bearing, high temperature, high salinity and high oxygen fugacity, begins to exsolve from magmatic melt due to the saturation of volatiles. The subsequent fluid boiling causes the precipitation of metals to form porphyry Cu and Mo mineralization in GPCB.

8. Conclusions

The Dabu deposit is a small-sized porphyry Cu–Mo deposit in the Gangdese porphyry copper belt (GPCB). The hydrothermal mineralization process includes three stages, namely stage I quartz–K-feldspar (biotite)±chalcopyrite ± pyrite veins, stage II quartz–molybdenite ± pyrite ± chalcopyrite veins, and stage III quartz–pyrite ± molybdenite veins. The ore-forming fluids are characterized by high temperature and high salinity, belonging to a H_2O–NaCl magmatic–hydrothermal system. The ore-forming materials show evidence of a magmatic origin related to the Miocene high Sr/Y intrusions in the GPCB, and boiling is the major factor in metal precipitation.

The estimated pressures of Qulong, Dabu and Zhunuo deposits are 16–42 MPa, 5–33 MPa, and 2–29 MPa, corresponding to mineralization depths of 1.6–4.3 km, 0.5–3.4 km and 0.2–3.0 km, respectively, displaying a gradually decreasing trend from eastern to western Gangdese. The relatively deep ore-forming depth and multiphase magmatic-hydrothermal activities are conducive to the formation of giant-sized porphyry deposits.

The ore-forming conditions of porphyry Cu–Mo deposits in GPCB, including mineralization depth and ore-fluid composition, are similar to those of porphyry Cu ± Au ± Mo deposits formed in oceanic subduction-related continental or island arcs (<4 km; NaCl-rich, CO_2-poor), but differ from those of porphyry Mo deposit formed in intracontinental collision regimes during or after orogenesis (>4 km; CO_2-rich, NaCl-poor). The inheritance of previously subduction-associated arc magma features through metamorphic dehydration and metasomatism of slab-derived fluid and oceanic sediments, without shallow crustal assimilation and input of the meteoric water during thickening and shortening, was responsible for the generation of post-collisional CO_2 poor, and Na, Cl enriched FIs associated with Miocene porphyry Cu-Mo deposits in Tibet.

Acknowledgments

We are grateful to three anonymous reviewers, Associate Editor Peter Lightfoot and Editor-in-Chief Franco Pirajno for their constructive comments and suggestions, which have largely improved this manuscript. Funding for this project was jointly granted by the Commonweal Project from the Ministry of Land and Resources, China (201511015), and Changjiang Scholars and Innovative Research Team in University (IRT14R54, IRT1083).

References

Ahmad, S.N., Rose, A.W., 1980. Fluid inclusions in porphyry and skarn ore at Santa Rita, New Mexico. Econ. Geol. 75, 229–250.
Asadi, S., Moore, F., Zarasvandi, A., 2014. Discriminating productive and barren porphyry copper deposits in the southeastern part of the central Iranian volcano–plutonic belt, Kerman region, Iran: a review. Earth Sci. Rev. 138, 25–46.

Audétat, A., Günther, D., 1999. Mobility and H_2O loss from fluid inclusions in natural quartz crystals. Contrib. Mineral. Petrol. 137, 1–14.
Azbej, T., Severs, M.J., Rusk, B.G., Bodnar, R.J., 2007. In situ quantitative analysis of individual H_2O-CO_2 fluid inclusions by laser Raman spectroscopy. Chem. Geol. 237, 255–263.
Becker, S.P., Fall, A., Bodnar, R.J., 2008. Synthetic fluid inclusions. XVII. PVTX properties of high salinity H_2O–NaCl solutions (>30 wt.% NaCl): application to fluid inclusions that homogenize by halite disappearance from porphyry copper and other hydrothermal ore deposits. Econ. Geol. 103, 539–554.
Bodnar, R.J., 1993. Revised equation and table for determining the freezing point depression of H_2O–NaCl solutions. Geochim. Cosmochim. Acta 57, 683–684.
Bodnar, R.J., Burnham, C.W., Sterner, S.M., 1985. Synthetic fluid inclusions in natural quartz. III. Determination of phase equilibrium properties in the system H_2O–NaCl to 1000 °C and 1500 bars. Geochim. Cosmochim. Acta 49, 1861–1873.
Bodnar, R.J., Lecumberri-Sanchez, P., Moncada, D., Steele-MacInnis, M., 2014. 13.5–fluid inclusions in hydrothermal ore deposits. In: Turekian, H.D.H.K. (Ed.), Treatise on Geochemistry (Second Edition). Elsevier, Oxford, pp. 119–142.
Bouzari, F., Clark, A.H., 2006. Prograde evolution and geothermal affinities of a major porphyry copper deposit: the Cerro Colorado hypogene protore, I Región, northern Chile. Econ. Geol. 101, 95–134.
Brown, P.E., Lamb, W.M., 1989. P-V-T properties of fluids in the system $H_2O \pm CO_2 \pm$ NaCl: new graphical presentations and implications for fluid inclusion studies. Geochim. Cosmochim. Acta 53, 1209–1221.
Brown, P.E., Hagemann, S.G., 1995. MacFlinCor and its application to fluids in Archean lode–gold deposits. Geochim. Cosmochim. Acta 59, 3943–3952.
Chaussidon, M., Albarède, F., Sheppard, S.M.F., 1989. Sulphur isotope variations in the mantle from ion microprobe analyses of micro-sulphide inclusions. Earth Planet. Sci. Lett. 92, 144–156.
Chen, L., Qin, K.Z., Li, G.M., Li, J.X., Xiao, B., Zhao, J.X., Fan, X., 2015. Zircon U-Pb ages, geochemistry, and Sr–Nd–Pb–Hf isotopes of the Nuri intrusive rocks in the Gangdese area, southern Tibet: constraints on timing, petrogenesis, and tectonic transformation. Lithos 212–215, 379–396.
Chen, Y., Ni, P., Fan, H., Pirajno, F., Lai, Y., Su, W., Zhang, H., 2007. Diagnostic fluid inclusions of different types hydrothermal gold deposits. Acta Petrol. Sin. 23, 2085–2108 (in Chinese with English abstract).
Chen, Y.J., Xiao, W.J., Zhang, J.J., 2008. Ore-system as a geodynamic probe. Chin. Geol. 35, 1059–1073 (in Chinese with English abstract).
Chen, Y.J., Li, N., 2009. Diagnostic fluid inclusion and wallrock alteration of intrusion-related hypothermal ore-systems (porphyry, skarn, breccia pipe, vein and IOCG) formed in intracontinental settings: origin and difference from those in volcanic arc. Acta Petrol. Sin. 25, 2477–2508 (in Chinese with English abstract).
Chen, Y.J., Wang, P., Li, N., Yang, Y.F., Pirajno, F., 2017. The collision-type porphyry Mo deposits in Dabie Shan, China. Ore Geol. Rev. 81, 405–430.
Chiaradia, M., 2013. Copper enrichment in arc magmas controlled by overriding plate thickness. Nat. Geosci. 7, 43–46.
Chung, S.L., Chu, M.F., Zhang, Y., Xie, Y., Lo, C.H., Lee, T.Y., Lan, C.Y., Li, X., Zhang, Q., Wang, Y., 2005. Tibetan tectonic evolution inferred from spatial and temporal variations in post-collisional magmatism. Earth Sci. Rev. 68, 173–196.
Chung, S.L., Chu, M.F., Ji, J., O'Reilly, S.Y., Pearson, N.J., Liu, D., Lee, T.Y., Lo, C.H., 2009. The nature and timing of crustal thickening in Southern Tibet: geochemical and zircon Hf isotopic constraints from postcollisional adakites. Tectonophysics 477, 36–48.
Clayton, R.N., Mayeda, T.K., 1963. The use of bromine pentafluoride in the extraction of oxygen from oxides and silicates for isotopic analysis. Geochim. Cosmochim. Acta 27, 43–52.
Clayton, R.N., O'Neil, J.R., Mayeda, T.K., 1972. Oxygen isotope exchange between quartz and water. J. Geophys. Res. 77, 3057–3067.
Cline, J.S., Bodnar, R.J., 1991. Can economic porphyry copper mineralization be generated by a typical calc-alkaline melt? J. Geophys. Res. 96, 8113–8126.
Cline, J.S., 1995. Genesis of porphyry copper deposits: The behavior of water, chloride, and copper in crystalline melts. In: Pierce, F.W., Bohm, G.J. (Eds.), Porphyry copper deposits in American Cordillera. Ariz Geol Soci Dig, pp. 69–82.
Coleman, M.L., Sheppard, T.J., Durham, J.J., Rouse, J.E., Moore, G.R., 1982. Reduction of water with zinc for hydrogen isotope analysis. Anal. Chem. 54, 993–995.
Core, D.P., Kesler, S.E., Essene, E.J., 2006. Unusually Cu-rich magmas associated with giant porphyry copper deposits: evidence from Bingham, Utah. Geology 34, 41–44.
Del Rio Salas, R., Ochoa-Landín, L., Ruiz, J., Eastoe, C., Meza-Figueroa, D., Zuñiga-Hernández, H., Mendívil-Quijada, H., Quintanar-Ruiz, F., 2013. Geology, stable isotope, and U-Pb geochronology of the Mariquita porphyry copper and Lucy Cu–Mo deposits, Cananea District, Mexico: a contribution to regional exploration. J. Geochem. Explor. 124, 140–154.
De Vivo, B., Lima, A., Webster, J.D., 2005. Volatiles in magmatic–volcanic systems. Elements 1, 19–24.
Defant, M.J., Drummond, M.S., 1993. Mount St. Helens: potential example of the partial melting of the subducted lithosphere in a volcanic arc. Geology 21, 547–550.
Dewey, J.F., Shackleton, R.M., Chang, C., Sun, Y., 1988. The tectonic evolution of the Tibetan Plateau. Philos. Trans. R. Soc. Lond. A 327, 379–413.
Dong, X., Zhang, Z., Santosh, M., 2010. Zircon U-Pb chronology of the Nyingtri group, southern Lhasa terrane, Tibetan Plateau: implications for Grenvillian and Pan-African provenance and Mesozoic-Cenozoic metamorphism. J. Geol. 118, 677–690.
Driesner, T., Heinrich, C.A., 2007. The system H_2O–NaCl. Part I: correlation formulae for phase relations in temperature-pressure-composition space from 0 to 1000 °C, 0 to 5000 bar, and 0 to 1 X_{NaCl}. Geochim. Cosmochim. Acta 71, 4880–4901.
Eastoe, C.J., 1983. Sulfur isotope data and the nature of the hydrothermal systems at the Panguna and Frieda porphyry copper deposits, Papua New Guinea. Econ. Geol. 78, 201–213.
Field, C.W., 1966. Sulfur isotope abundance data, Bingham district, Utah. Econ. Geol. 61, 850–871.
Field, C.W., Gustafson, L.B., 1976. Sulfur isotopes in the porphyry copper deposit at El Salvador, Chile. Econ. Geol. 71, 1533–1548.
Field, C.W., Zhang, L., Dilles, J.H., Rye, R.O., Reed, M.H., 2005. Sulfur and oxygen isotopic record in sulfate and sulfide minerals of early, deep, pre-Main Stage porphyry Cu–Mo and late Main Stage base-metal mineral deposits, Butte district, Montana. Chem. Geol. 215, 61–93.
Gao, S.B., Zheng, Y.Y., 2006. Geochemical controlling of mineralization in Qulong super large porphyry copper deposit, Tibet. Geol. Sci. Technol. Inf. 25, 41–46 (in Chinese with English abstract).
Gao, Y., Yang, Z., Santosh, M., Hou, Z., Wei, R., Tian, S., 2010. Adakitic rocks from slab melt-modified mantle sources in the continental collision zone of southern Tibet. Lithos 119, 651–663.
Geologic Exploration Team of Geological Survey Institute of Tibet, China, 2011. Exploration design of Dabu Cu-Mo deposit in Quxu County (in Chinese).
Gregory, M.J., 2017. A fluid inclusion and stable isotope study of the Pebble porphyry copper-gold-molybdenum deposit, Alaska. Ore Geol. Rev. 80, 1279–1303.
Guo, Z., Wilson, M., Zhang, M., Cheng, Z., Zhang, L., 2015. Post-collisional Ultrapotassic Mafic Magmatism in South Tibet: products of partial melting of pyroxenite in the mantle wedge induced by roll-back and delamination of the subducted Indian Continental Lithosphere Slab. J. Petrol. 56, 1365–1406.
Gustafson, L.B., Quiroga, J., 1995. Patterns of mineralization and alteration below the porphyry copper orebody at El Salvador, Chile. Econ. Geol. 90, 2–16.
Guynn, J., Kapp, P., Gehrels, G.E., Ding, L., 2012. U-Pb geochronology of basement rocks in central Tibet and paleogeographic implications. J. Asian Earth Sci. 43, 23–50.
Haas, J.L., 1976. Physical properties of the coexisting phases and thermodynamic properties of the H2O component in boiling NaCl solutions. U.S. Geol. Surv. Bull. 1421-A, 73.
Halter, W.E., Heinrich, C.A., Pettke, T., 2005. Magma evolution and the formation of porphyry Cu–Au ore fluids: evidence from silicate and sulfide melt inclusions. Miner. Deposita 39, 845–863.
Harris, A.C., Golding, S.D., White, N.C., 2005. Bajo de la Alumbrera copper-gold deposit: stable isotope evidence for a porphyry-related hydrothermal system dominated by magmatic aqueous fluids. Econ. Geol. 100, 863–886.
Haschke, M., Ahmadian, J., Murata, M., McDonald, I., 2010. Copper mineralization prevented by arc-root delamination during Alpine-Himalayan collision in central Iran. Econ. Geol. 105, 855–865.
Hedenquist, J.W., Arribas, R., Aoki, M., 2017. Zonation of sulfate and sulfide minerals and isotopic composition in the far southeast porphyry and lepanto epithermal Cu–Au deposits, Philippines. Resour. Geol. 67, 174–196.
Hoefs, J., 2009. Stable Isotope Geochemistry. Springer-Verlag, Berlin Heidelberg, pp. 1–285.
Hou, Z.Q., Yang, Z.M., Qu, X.M., Meng, X.J., Li, Z.Q., Beaudoin, G., Rui, Z.Y., Gao, Y.F., Zaw, K., 2009. The Miocene Gangdese porphyry copper belt generated during post-collisional extension in the Tibetan Orogen. Ore Geol. Rev. 36, 25–51.
Hou, Z., Zhang, H., Pan, X., Yang, Z., 2011. Porphyry Cu (–Mo–Au) deposits related to melting of thickened mafic lower crust: examples from the eastern Tethyan metallogenic domain. Ore Geol. Rev. 39, 21–45.
Hou, Z.Q., Duan, L.F., Lu, Y.J., Zheng, Y.C., Zhu, D.C., Yang, Z.M., Yang, Z.S., Wang, B.D., Pei, Y.R., Zhao, Z.D., 2015a. Lithospheric architecture of the Lhasa Terrane and its control on ore deposits in the Himalayan-Tibetan Orogen. Econ. Geol. 110, 1541–1575.
Hou, Z.Q., Yang, Z.M., Lu, Y.J., Kemp, A., Zheng, Y.C., Li, Q.Y., Tang, J.X., Yang, Z.S., Duan, L.F., 2015b. A genetic linkage between subduction- and collision-related porphyry Cu deposits in continental collision zones. Geology 43, 247–250.
Hou, Z.Q., Zhang, H.R., 2015. Geodynamics and metallogeny of the eastern Tethyan metallogenic domain. Ore Geol. Rev. 70, 346–384.
Hu, Y.B., Liu, J.Q., Ling, M.X., Ding, W., Liu, Y., Zartman, R.E., Ma, X.F., Liu, D.Y., Zhang, C.C., Sun, S.J., Zhang, L.P., Wu, K., Sun, W.D., 2015. The formation of Qulong adakites and their relationship with porphyry copper deposit: geochemical constraints. Lithos 220–223, 60–80.
Imai, A., 2005. Evolution of hydrothermal system at the Dizon Porphyry Cu-Au Deposit, Zambales, Philippines. Resour. Geol. 55, 73–90.
Jahangiri, A., 2007. Post-collisional Miocene adakitic volcanism in NW Iran: geochemical and geodynamic implications. J. Asian Earth Sci. 30, 433–447.
Ji, W.Q., Wu, F.Y., Chung, S.L., Li, J.X., Liu, C.Z., 2009. Zircon U-Pb geochronology and Hf isotopic constraints on petrogenesis of the Gangdese batholith, southern Tibet. Chem. Geol. 262, 229–245.
Klemm, L.M., Pettke, T., Heinrich, C.A., 2008. Fluid and source magma evolution of the Questa porphyry Mo deposit, New Mexico, USA. Miner. Deposita 43, 533–552.
Kouzmanov, K., Ramboz, C., Lerouge, C., Deloule, E., Beaufort, D., Bogdanov, K., 2003. Stable isotopic constrains on the origin of epithermal Cu–Au and related porphyry copper mineralizations in the southern Panagyurishte district, Srednogorie zone, Bulgaria. In: Eliopoulos, D.G. et al. (Eds.), Mineral Exploration and Sustainable Development. Millpress, Rotterdam, pp. 1181–1184.
Landtwing, M.R., Furrer, C., Redmond, P.B., Pettke, T., Guillong, M., Heinrich, C.A., 2010. The Bingham Canyon porphyry Cu-Mo-Au deposit. III. Zoned copper-gold ore deposition by magmatic vapor expansion. Econ. Geol. 105, 91–118.

Lange, I.M., Cheney, E.S., 1971. Sulfur isotope reconnaissance of Butte, Montana. Econ. Geol. 66, 63–74.
Lee, C.T.A., 2013. Economic geology: copper conundrums. Nat. Geosci. 7, 10–11.
Lee, C.T.A., Luffi, P., Chin, E.J., Bouchet, R., Dasgupta, R., Morton, D.M., Le Roux, V., Yin, Q.z., Jin, D., 2012b. Copper systematics in arc magmas and implications for crust-mantle differentiation. Science 336, 64–68.
Lee, H.Y., Chung, S.L., Ji, J., Qian, Q., Gallet, S., Lo, C.H., Lee, T.Y., Zhang, Q., 2012a. Geochemical and Sr–Nd isotopic constraints on the genesis of the Cenozoic Linzizong volcanic successions, southern Tibet. J. Asian Earth Sci. 53, 96–114.
Li, X., Wang, C., Mao, W., Xu, Q., Liu, Y., 2014a. The fault-controlled skarn W-Mo polymetallic mineralization during the main India-Eurasia collision: example from Hahaigang deposit of Gangdese metallogenic belt of Tibet. Ore Geol. Rev. 58, 27–40.
Li, H., Ye, H., Wang, X., Yang, L., Wang, X., 2014b. Geology and ore fluid geochemistry of the Jinduicheng porphyry molybdenum deposit, East Qinling, China. J. Asian Earth Sci. 79, 641–654.
Li, Y., Xie, Y., Chen, W., Tang, Y., Li, G., Zhang, L., Liu, Y., Liu, X., 2011a. U-Pb age and geochemical characteristics of zircon in monzogranite porphyry from Qiagong deposit, Tibet, and geological implication. Acta Petrol. Sin. 27, 2023–2033 (in Chinese with English abstract).
Li, J.X., Qin, K.Z., Li, G.M., Xiao, B., Chen, L., Zhao, J.X., 2011b. Post-collisional ore-bearing adakitic porphyries from Gangdese porphyry copper belt, southern Tibet: melting of thickened juvenile arc lower crust. Lithos 126, 265–277.
Li, M., Sun, X., Zheng, Y., Guo, F., 2015. Characteristic of fluid inclusions of the Zhunuo porphyry copper deposit in the Gangdese belt, Tibet. Acta Petrol. Sin. 31, 1335–1347 (in Chinese with English abstract).
Li, Y., Selby, D., Feely, M., Costanzo, A., Li, X.H., 2017. Fluid inclusion characteristics and molybdenite Re–Os geochronology of the Qulong porphyry copper-molybdenum deposit, Tibet. Miner. Deposita 52, 137–158.
Liu, D., Zhao, Z., Zhu, D.C., Niu, Y., DePaolo, D.J., Mark Harrison, T., Mo, X., Dong, G., Zhou, S., Sun, C., Zhang, Z., Liu, J., 2014a. Postcollisional potassic and ultrapotassic rocks in southern Tibet: mantle and crustal origins in response to India-Asia collision and convergence. Geochim. Cosmochim. Acta 143, 207–231.
Liu, D., Zhao, Z., DePaolo, D.J., Zhu, D.C., Meng, F.Y., Shi, Q., Wang, Q., 2017. Potassic volcanic rocks and adakitic intrusions in southern Tibet: insights into mantle–crust interaction and mass transfer from Indian plate. Lithos 268, 48–64.
Liu, J., Mao, J.W., Wu, G., Wang, F., Luo, D.F., Hu, Y.Q., Li, T.G., 2014b. Fluid inclusions and H-O–S–Pb isotope systematics of the Chalukou giant porphyry Mo deposit, Heilongjiang Province, China. Ore Geol. Rev. 59, 83–96.
Loucks, R.R., 2014. Distinctive composition of copper-ore-forming arc magmas. Aust. J. Earth Sci. 61, 5–16.
Lu, H.Z., 2000. High temperature, salinity and high concentrated ore metal magmatic fluids: an example from Grasberg Cu-Au porphyry deposit. Acta Petrol. Sin. 16, 465–472 (in Chinese with English abstract).
Lu, Y.J., Loucks, R.R., Fiorentini, M.L., Yang, Z.M., Hou, Z.Q., 2015. Fluid flux melting generated postcollisional high Sr/Y copper ore-forming water-rich magmas in Tibet. Geology 43, 583–586.
Lu, Y.J., Loucks, R.R., Fiorentini, M., McCuaig, T.C., Evans, N.J., Yang, Z.M., Hou, Z.Q., Kirkland, C.L., Parra-Avila, L.A., Kobussen, A., 2016. Zircon Compositions as a Pathfinder for Porphyry Cu ± Mo ± Au Deposits. Soc. Econ. Geol. Spec. Publ. 19, 329–347.
Mao, J.W., Pirajno, F., Lehmann, B., Luo, M.C., Berzina, A., 2014. Distribution of porphyry deposits in the Eurasian continent and their corresponding tectonic settings. J. Asian Earth Sci. 79, 576–584.
Maydagán, L., Franchini, M., Lentz, D., Pons, J., McFarlane, C., 2013. Sulfide composition and isotopic signature of the Altar Cu-Au deposit, Argentina: constraints on the evolution of the porphyry-epithermal system. Can. Mineral. 51, 813–840.
Meng, X., Hou, Z., Li, Z., 2006. Sulfur and lead isotope compositions of the Qulong porphyry copper deposit, Tibet: implications for the sources of plutons and metals in the deposit. Acta Geol. Sin. 80, 560–569 (in Chinese with English abstract).
Meyer, Charles, Hemley, J.J., 1967. Wall rock alteration. In: Barnes, H.L. (Ed.), Geochemistry of Hydrothermal Ore Deposits. Holt, Rinehart, and Winston Inc, New York, pp. 166–235.
Miller, C., Schuster, R., Klötzli, U., Frank, W., Purtscheller, F., 1999. Post-collisional potassic and ultrapotassic magmatism in SW Tibet: geochemical and Sr–Nd–Pb–O isotopic constraints for mantle source characteristics and petrogenesis. J. Petrol. 40, 1399–1424.
Mo, X., Niu, Y., Dong, G., Zhao, Z., Hou, Z., Zhou, S., Ke, S., 2008. Contribution of syncollisional felsic magmatism to continental crust growth: a case study of the Paleogene Linzizong volcanic Succession in southern Tibet. Chem. Geol. 250, 49–67.
Murakami, H., Seo, J.H., Heinrich, C.A., 2010. The relation between Cu/Au ratio and formation depth of porphyry-style Cu–Au ± Mo deposits. Miner. Deposita 45, 11–21.
Ni, P., Wang, G.G., Yu, W., Chen, H., Jiang, L.L., Wang, B.H., Zhang, H.D., Xu, Y.F., 2015. Evidence of fluid inclusions for two stages of fluid boiling in the formation of the giant Shapinggou porphyry Mo deposit, Dabie Orogen, Central China. Ore Geol. Rev. 65, 1078–1094.
Nomade, S., Renne, P.R., Mo, X., Zhao, Z., Zhou, S., 2004. Miocene volcanism in the Lhasa block, Tibet: spatial trends and geodynamic implications. Earth Planet. Sci. Lett. 221, 227–243.
Ohmoto, H., 1972. Systematics of sulfur and carbon isotopes in hydrothermal ore deposits. Econ. Geol. 67, 551–578.
Ohmoto, H., Rye, R.O., 1979. Isotopes of sulfur and carbon. In: Barnes, H.L. (Ed.), Geochemistry of Hydrothermal Ore Deposits. second ed. JohnWiley and Sons, New York, pp. 509–567.
Omrani, J., Agard, P., Whitechurch, H., Benoit, M., Prouteau, G., Jolivet, L., 2008. Arc-magmatism and subduction history beneath the Zagros Mountains, Iran: a new report of adakites and geodynamic consequences. Lithos 106, 380–398.
Pan, G.T., Ding, J., Yao, D.S., Wang, L.Q., 2004. Guidebook of 1: 1,500,000 Geologic Map of the Qinghai-Xizang (Tibet) Plateau and Adjacent Areas. Cartographic Publishing House, Chengdu, China, pp. 1–148 (in Chinese).
Pan, G.T., Mo, X.X., Hou, Z.Q., Zhu, D.C., Wang, L.Q., Li, G.M., Zhao, Z.D., Geng, Q.R., Liao, Z.L., 2006. Spatial-temporal framework of the Gangdese Orogenic Belt and its evolution. Acta Petrol. Sin. 22, 521–533 (in Chinese with English abstract).
Pirajno, F., 2009. Hydrothermal Processes and Mineral Systems. Springer, Berlin (1250 pp).
Qin, K.Z., 2012. Thematic Articles "Porphyry Cu–Au–Mo deposits in Tibet and Kazakhstan". Resour. Geol. 62, 1–3.
Qu, X.M., Hou, Z.Q., Li, Y.Q., 2004. Melt components derived from a subducted slab in late orogenic ore-bearing porphyries in the Gangdese copper belt, southern Tibetan plateau. Lithos 74, 131–148.
Qu, X.M., Hou, Z.Q., Khin, Z., Li, Y.G., 2007. Characteristics and genesis of Gangdese porphyry copper deposits in the southern Tibetan Plateau: preliminary geochemical and geochronological results. Ore Geol. Rev. 31, 205–223.
Redmond, P.B., Einaudi, M.T., Inan, E.E., et al., 2004. Copper deposition by fluid cooling in intrusion-centered systems: new insights from the Bingham porphyry ore deposit, Utah. Geology 32, 217–220.
Richards, J.P., 2003. Tectono-magmatic precursors for porphyry Cu–(Mo–Au) deposit formation. Econ. Geol. 98, 1515–1533.
Richards, J.P., 2011a. High Sr/Y arc magmas and porphyry Cu ± Mo ± Au deposits: just add water. Econ. Geol. 106, 1075–1081.
Richards, J.P., 2011b. Magmatic to hydrothermal metal fluxes in convergent and collided margins. Ore Geol. Rev. 40, 1–26.
Richards, J.P., Spell, T., Rameh, E., Razique, A., Fletcher, T., 2012. High Sr/Y magmas reflect arc maturity, high magmatic water content, and porphyry Cu ± Mo ± Au potential: examples from the Tethyan arcs of Central and Eastern Iran and Western Pakistan. Econ. Geol. 107, 295–332.
Richards, J.P., 2013. Giant ore deposits formed by optimal alignments and combinations of geological processes. Nat. Geosci. 6, 911–916.
Richards, J.P., 2015. Tectonic, magmatic, and metallogenic evolution of the Tethyan orogen: from subduction to collision. Ore Geol. Rev. 70, 323–345.
Robinson, B.W., Kusakabe, M., 1975. Quantitative preparation of sulfur dioxide, for sulfur-34/sulfur-32 analyses, from sulfides by combustion with cuprous oxide. Anal. Chem. 47, 1179–1181.
Roedder, E., Bodnar, R.J., 1980. Geologic pressure determinations from fluid inclusion studies. Ann. Rev. Earth Planet. Sci. 8, 263.
Roedder, E., 1984. Fluid inclusions. Rev. Mineral. 12, 1–644.
Rusk, B.G., Reed, M.H., Dilles, J.H., Klemm, L.M., Heinrich, C.A., 2004. Compositions of magmatic hydrothermal fluids determined by LA–ICP–MS of fluid inclusions from the porphyry copper–molybdenum deposit at Butte, MT. Chem. Geol. 210, 173–199.
Rusk, B.G., Reed, M.H., Dilles, J.H., 2008. Fluid inclusion evidence for magmatic-hydrothermal fluid evolution in the porphyry copper-molybdenum deposit at Butte, Montana. Econ. Geol. 103, 307–334.
Rye, R.O., 1993. The evolution of magmatic fluids in the epithermal environment; the stable isotope perspective. Econ. Geol. 88, 733–752.
Seo, J.H., Guillong, M., Heinrich, C.A., 2012. Separation of molybdenum and copper in porphyry deposits: the roles of sulfur, redox, and pH in ore mineral deposition at Bingham Canyon. Econ. Geol. 107, 333–356.
Shafiei, B., Haschke, M., Shahabpour, J., 2009. Recycling of orogenic arc crust triggers porphyry Cu mineralization in Kerman Cenozoic arc rocks, southeastern Iran. Miner. Deposita 44, 265–283.
She, H.Q., Feng, C.Y., Zhang, D.Q., Pan, G.T., Li, G.M., 2005. Characteristics and metallogenetic potential of skarn copper–lead–zinc polymetallic deposits in central eastern Gangdese. Miner. Deposits 24, 508–520 (in Chinese with English abstract).
Shepherd, T.J., Rankin, A.H., Alderton, D., 1985. A Practical Guide to Fluid Inclusion Studies. Blackie & Son, Glasgow, p. 239.
Shu, Q., Lai, Y., Sun, Y., Wang, C., Meng, S., 2013. Ore genesis and hydrothermal evolution of the Baiyinnuo'er zinc-lead skarn deposit, northeast China: evidence from isotopes (S, Pb) and fluid inclusions. Econ. Geol. 108, 835–860.
Sillitoe, R.H., 1972. A plate tectonic model for the origin of porphyry copper deposits. Econ. Geol. 67, 184–197.
Sillitoe, R.H., 2010. Porphyry copper systems. Econ. Geol. 105, 3–41.
Simon, G., Kesler, S.E., Essene, E.J., Chryssoulis, S.L., 2000. Gold in porphyry copper deposits: Experimental determination of the distribution of gold in the Cu-Fe-S system at 400 to 700 °C. Econ. Geol. 95, 259–270.
Singer, D.A., Berger, V.I., Moring, B.C., 2005. Porphyry copper deposits of the world: database, map, and grade and tonnage models. U.S. Geological Survey Open-File Report 2005–1060.
Sterner, S.M., Hall, D.L., Bodnar, R.J., 1988. Synthetic fluid inclusions. V. Solubility relations in the system NaCl-KCl-H_2O under vapor-saturated conditions. Geochim. Cosmochim. Acta 52, 989–1005.
Sun, W.D., Liang, H.Y., Ling, M.X., Zhan, M.Z., Ding, X., Zhang, H., Yang, X.Y., Li, Y.L., Ireland, T.R., Wei, Q.R., Fan, W.M., 2013a. The link between reduced porphyry copper deposits and oxidized magmas. Geochim. Cosmochim. Acta 103, 263–275.
Sun, X., Zheng, Y., Wu, S., You, Z., Wu, X., Li, M., Zhou, T., Dong, J., 2013b. Mineralization age and petrogenesis of associated intrusions in the Mingze-

Chengba porphyry-skarn Mo-Cu deposit, Gangdese. Acta Petrol. Sin. 29, 1392–1406 (in Chinese with English abstract).
Sun, X., Zheng, Y., Xu, J., Huang, L., Guo, F., Gao, S., 2017. Metallogenesis and ore controls of Cenozoic porphyry Mo deposits in the Gangdese belt of southern Tibet. Ore Geol. Rev. 81, 996–1014.
Tan, G., She, H.Q., Yin, J.P., Yang, Y.C., Li, J.W., Xiang, A.P., 2013. Source and evolution of ore-fluid in Wunugetushan large Cu–Mo deposit, Inner Mongolia: evidence from fluid inclusions and hydrogen and oxygen isotopic geochemistry. Glob. Geol. 32, 463–482 (in Chinese with English abstract).
Tang, H.C., 2015. The comparative study of characteristics of petrogenesis and metallogeny for Nannihu and Shangfanggou in Luanchuan ore-concentration area (Master's thesis) China University of Geosciences, Beijing (77pp, in Chinese with English abstract).
Tang, H.S., Chen, Y.J., Wu, G., Lai, Y., 2008. The C-O isotope composition of the Liaohe Group, northern Liaoning province and its geologic implications. Acta Petrol. Sin. 24, 129–138 (in Chinese with English abstract).
Tang, H.S., Wu, G., Lai, Y., 2009. The C-O isotope geochemistry and genesis of the Dashiqiao magnesite deposit, Liaoning province, NE China. Acta Petrol. Sin. 25, 455–467 (in Chinese with English abstract).
Taylor, H.P., 1974. The application of oxygen and hydrogen isotope studies to problems of hydrothermal alteration and ore deposition. Econ. Geol. 69, 843–883.
Turner, S., Arnaud, N., Liu, J., Rogers, N., Hawkesworth, C., Harris, N., Kelley, S., Van Calsteren, P., Deng, W., 1996. Post-collision, shoshonitic volcanism on the Tibetan Plateau: implications for convective thinning of the lithosphere and the source of ocean island basalts. J. Petrol. 37, 45–71.
Ulrich, T., Guenther, D., Heinrich, C.A., 1999. Gold concentrations of magmatic brines and the metal budget of porphyry copper deposits. Nature 399, 676–679.
Ulrich, T., Günther, D., Heinrich, C.A., 2001. The evolution of a porphyry Cu-Au deposit, based on LA-ICP-MS analysis of fluid inclusions: Bajo de la Alumbrera, Argentina. Econ. Geol. 96, 1743–1774.
Urusova, M.A., 1975. Volume properties of aqueous solutions of sodium chloride at elevated temperatures and pressures. Russ. J. Inorg. Chem. 20, 1717–1721.
Wang, L., Mo, X., Li, B., Dong, G., Zhao, Z., 2006. Geochronology and geochemistry of the ore-bearing porphyry in Qulong Cu (Mo) ore deposit, Tibet. Acta Petrol. Sin. 22, 1001–1008 (in Chinese with English abstract).
Wang, R., Richards, J.P., Hou, Z.Q., Yang, Z.M., 2014a. Extent of underthrusting of the Indian plate beneath Tibet controlled the distribution of Miocene porphyry Cu–Mo ± Au deposits. Miner. Deposita 49, 165–173.
Wang, R., Richards, J.P., Hou, Z.Q., Yang, Z.M., DuFrane, S.A., 2014b. Increased magmatic water content—The key to Oligo-Miocene Porphyry Cu-Mo ± Au formation in the Eastern Gangdese Belt, Tibet. Econ. Geol. 109, 1315–1339.
Wang, R., Richards, J.P., Hou, Z.Q., Yang, Z.M., Gou, Z.B., DuFrane, S.A., 2014c. Increasing magmatic oxidation state from Paleocene to Miocene in the Eastern Gangdese Belt, Tibet: implication for collision-related Porphyry Cu–Mo ± Au mineralization. Econ. Geol. 109, 1943–1965.
Wang, P., Chen, Y.J., Fu, B., Yang, Y.F., Mi, M., Li, Z.L., 2014d. Fluid inclusion and H-O–C isotope geochemistry of the Yaochong porphyry Mo deposit in Dabie Shan, China: a case study of porphyry systems in continental collision orogens. Int. J. Earth Sci. 103, 777–797.
Wang, R., Richards, J.P., Zhou, L.M., Hou, Z.Q., Stern, R.A., Creaser, R.A., Zhu, J.J., 2015a. The role of Indian and Tibetan lithosphere in spatial distribution of Cenozoic magmatism and porphyry Cu–Mo deposits in the Gangdese belt, southern Tibet. Earth Sci. Rev. 150, 68–94.
Wang, L., Tang, J., Cheng, W., Chen, W., Zhang, Z., Lin, X., Luo, M., Yang, C., 2015b. Origin of the ore-forming fluids and metals of the Bangpu porphyry Mo–Cu deposit of Tibet, China: constraints from He–Ar, H-O, S and Pb isotopes. J. Asian Earth Sci. 103, 276–287.
Wang, Y.Y., Tang, J.X., Zheng, W.B., Duan, J.L., Song, J.L., Yang, C., 2015c. Mechanism of metal precipitation in Dabu porphyry Cu–Mo deposit, Quxu Country, Tibet. Miner. Deposits 34, 81–97 (in Chinese with English abstract).
Wen, D.R., Chung, S.L., Song, B., Iizuka, Y., Yang, H.J., Ji, J., Liu, D., Gallet, S., 2008. Late Cretaceous Gangdese intrusions of adakitic geochemical characteristics, SE Tibet: petrogenesis and tectonic implications. Lithos 105, 1–11.
Wilkinson, J.J., 2001. Fluid inclusions in hydrothermal ore deposits. Lithos 55, 229–272.
Williams, H.M., Turner, S.P., Pearce, J.A., Kelley, S.P., Harris, N.B.W., 2004. Nature of the source regions for post-collisional, potassic magmatism in southern and northern Tibet from geochemical variations and inverse trace element modelling. J. Petrol. 45, 555–607.
Wu, S., Zheng, Y.Y., Sun, X., Liu, S.A., Geng, R.R., You, Z.M., Ouyang, H.T., Lei, D., Zhao, Z.Y., 2014. Origin of the Miocene porphyries and their mafic microgranular enclaves from Dabu porphyry Cu–Mo deposit, southern Tibet: implications for magma mixing/mingling and mineralization. Int. Geol. Rev. 56, 571–595.
Wu, S., Zheng, Y.Y., Sun, X., 2016. Subduction metasomatism and collision-related metamorphic dehydration controls on the fertility of porphyry copper ore-forming high Sr/Y magma in Tibet. Ore Geol. Rev. 73, 83–103.
Xiao, B., Qin, K., Li, G., Li, J., Xia, D., Chen, L., Zhao, J., 2012. Highly oxidized magma and fluid evolution of Miocene Qulong Giant Porphyry Cu–Mo Deposit, Southern Tibet, China. Resour. Geol. 62, 4–18.
Xu, R.H., Schärer, U., Allègre, C.J., 1985. Magmatism and metamorphism in the Lhasa block (Tibet): a geochronological study. J. Geol. 93, 41–57.
Yang, Y.F., Chen, Y.J., Li, N., Mi, M., Xu, Y.L., Li, F.L., Wan, S.Q., 2013. Fluid inclusion and isotope geochemistry of the Qian'echong giant porphyry Mo deposit, Dabie Shan, China: a case of NaCl-poor, CO_2-rich fluid systems. J. Geochem. Explor. 124, 1–13.
Yang, Y.F., Chen, Y.J., Pirajno, F., et al., 2015b. Evolution of ore fluids in the Donggou giant porphyry Mo system, East Qinling, China, a new type of porphyry Mo deposit: evidence from fluid inclusion and H-O isotope systematics. Ore Geol. Rev. 65 (Part 1), 148–164.
Yang, Z.M., 2008. The Qulong Giant Porphyry Copper Deposit in Tibet: Magmatism and Mineralization (Ph. D. thesis) Institute of Geology Chinese Academy of Geological Sciences, Beijing (144 pp., in Chinese with English abstract).
Yang, Z.M., Hou, Z.Q., White, N.C., Chang, Z.S., Li, Z.Q., Song, Y.C., 2009. Geology of the post-collisional porphyry copper–molybdenum deposit at Qulong, Tibet. Ore Geol. Rev. 36, 133–159.
Yang, Z.M., Lu, Y.J., Hou, Z.Q., Chang, Z.S., 2015a. High-Mg Diorite from Qulong in Southern Tibet: implications for the genesis of adakite-like intrusions and associated Porphyry Cu Deposits in collisional orogens. J. Petrol. 56, 227–254.
Yin, A., Harrison, T.M., 2000. Geologic evolution of the Himalayan-Tibetan Orogen. Annu. Rev. Earth Planet. Sci. 28, 211–280.
Zartman, R.E., Doe, B.R., 1981. Plumbotectonics—the model. Tectonophysics 75, 135–162.
Zeng, Y.C., Chen, J.L., Xu, J.F., Lei, M., Xiong, Q.W., 2017. Origin of Miocene Cu-bearing porphyries in the Zhunuo region of the southern Lhasa subterrane: constraints from geochronology and geochemistry. Gondwana Res. 41, 51–64.
Zhang, L., 2000. Stable Isotope Investigation of a Hydrothermal Alteration System—Butte Porphyry Copper Deposit (Ph. D. thesis) Oregon State University, Corvallis.
Zhang, Q.L., Qu, X.M., Xu, W.Y., Hou, Z.Q., Chen, W.S., 2003. Study of the fluid inclusions from Nanmu porphyry Cu-Mo deposit in Tibet. Acta Petrol. Sin. 19, 251–259 (in Chinese with English abstract).
Zhang, Z.M., Dong, X., Santosh, M., Zhao, G.C., 2014. Metamorphism and tectonic evolution of the Lhasa terrane, Central Tibet. Gondwana Res. 25, 170–189.
Zhao, J., Qin, K., Li, G., Li, J., Xiao, B., Chen, L., Yang, Y., Li, C., Liu, Y., 2014. Collision-related genesis of the Sharang porphyry molybdenum deposit, Tibet: evidence from zircon U-Pb ages, Re–Os ages and Lu–Hf isotopes. Ore Geol. Rev. 56, 312–326.
Zhao, X., Yang, Z., Zheng, Y., Liu, Y., Tian, S., Fu, Q., 2015. Geology and genesis of the post-collisional porphyry–skarn deposit at Bangpu, Tibet. Ore Geol. Rev. 70, 486–509.
Zhao, Z., Mo, X., Dilek, Y., Niu, Y., DePaolo, D.J., Robinson, P., Zhu, D., Sun, C., Dong, G., Zhou, S., 2009. Geochemical and Sr–Nd–Pb–O isotopic compositions of the post-collisional ultrapotassic magmatism in SW Tibet: petrogenesis and implications for India intra-continental subduction beneath southern Tibet. Lithos 113, 190–212.
Zheng, Y.C., Fu, Q., Hou, Z.Q., Yang, Z.S., Huang, K.X., Wu, C.D., Sun, Q.Z., 2015b. Metallogeny of the northeastern Gangdese Pb–Zn–Ag–Fe–Mo–W polymetallic belt in the Lhasa terrane, southern Tibet. Ore Geol. Rev. 70, 510–532.
Zheng, Y.C., Hou, Z.Q., Li, W., Liang, W., Huang, K.X., Li, Q.Y., Sun, Q.Z., Fu, Q., Zhang, S., 2012a. Petrogenesis and geological implications of the oligocene chongmuda-mingze adakite-like intrusions and their Mafic Enclaves, Southern Tibet. J. Geol. 120, 647–669.
Zheng, Y.Y., Gao, S.B., Zhang, D.Q., Zhang, G.Y., Ma, G.T., Cheng, S.B., 2006. Ore-forming fluid controlling mineralization in Qulong super-large porphyry copper deposit, Tibet. Earth Sci. 31, 349–354 (in Chinese with English abstract).
Zheng, Y.Y., Gao, S.B., Sun, X., Zhang, G.Y., 2013. The Super-Large Qulong Porphyry Cu-Mo Deposit. Geology Publishing House, Beijing, p. 203.
Zheng, Y.Y., Sun, X., Gao, S.B., Wang, C.M., Zhao, Z.Y., Wu, S., Li, J.D., Wu, X., 2014. Analysis of stream sediment data for exploring the Zhunuo porphyry Cu deposit, southern Tibet. J. Geochem. Explor. 143, 19–30.
Zheng, Y.Y., Sun, X., Gao, S.B., Wu, S., Xu, J., Jiang, J.S., Chen, X., Zhao, Z.Y., Liu, Y., 2015a. Metallogenesis and the minerogenetic series in the Gangdese polymetallic copper belt. J. Asian Earth Sci. 103, 23–39.
Zheng, Y.Y., Sun, X., Zheng, H.T., Zhang, L.X., Ke, X.Z., Zheng, L., Yao, X., 2012b. Magma evolution of small intrusion and mineralization in Gangdese, Tibet. North Geol. 45, 165–174 (in Chinese with English abstract).
Zheng, Y.Y., Wang, B.S., Fan, Z.H., Zhang, H.P., 2002. Analysis of tectonic evolution in the eastern section of the Gangdise Mountains, Tibet and the metallogenic potentialities of copper–gold–polymetal. Geol. Sci. Technol. Inf. 21, 55–60 (in Chinese with English abstract).
Zheng, Y.Y., Xue, Y.X., Cheng, L.J., Fan, Z.H., Gao, S.B., 2004. Finding, characteristics and significances of qulong superlarge Porphyry Copper (Molybdenum) deposit, Tibet. Earth Sci. 29, 103–108 (in Chinese with English abstract).
Zheng, Y.Y., Zhang, G.Y., Xu, R.K., Gao, S.B., Pang, Y.C., Cao, L., Du, A.D., Shi, Y.R., 2007. Geochronologic constraints on magmatic intrusions and mineralization of the Zhunuo porphyry copper deposit in Gangdese, Tibet. Chin. Sci. Bull. 52, 3139–3147 (in Chinese with English abstract).
Zhu, D.C., Mo, X.X., Niu, Y., Zhao, Z.D., Wang, L.Q., Liu, Y.S., Wu, F.Y., 2009. Geochemical investigation of Early Cretaceous igneous rocks along an east–west traverse throughout the central Lhasa Terrane, Tibet. Chem. Geol. 268, 298–312.
Zhu, D.C., Zhao, Z.D., Niu, Y., Mo, X.X., Chung, S.L., Hou, Z.Q., Wang, L.Q., Wu, F.Y., 2011a. The Lhasa Terrane: record of a microcontinent and its histories of drift and growth. Earth Planet. Sci. Lett. 301, 241–255.
Zhu, D.C., Zhao, Z.D., Niu, Y., Dilek, Y., Mo, X.X., 2011b. Lhasa terrane in southern Tibet came from Australia. Geology 39, 727–730.
Zhu, D.C., Zhao, Z.D., Niu, Y., Dilek, Y., Hou, Z.Q., Mo, X.X., 2013. The origin and pre-Cenozoic evolution of the Tibetan Plateau. Gondwana Res. 23, 1429–1454.